Rotavirus Calcium Dysregulation Manifests as Dynamic Calcium Signaling in the Cytoplasm and Endoplasmic Reticulum

Alexandra L. Chang-Graham[1], Jacob L. Perry[1], Alicia C. Strtak[1], Nina K. Ramachandran[1], Jeanette M. Criglar[1], Asha A. Philip[3], John T. Patton[3], Mary K. Estes[1,2], and Joseph M. Hyser[1]*

[1]Alkek Center for Metagenomic and Microbiome Research; Department of Molecular Virology and Microbiology; [2]Department of Medicine, Gastroenterology and Hepatology, Baylor College of Medicine, Houston, TX 77303. [3]Department of Biology, Indiana University, Bloomington, IN 47405

*Correspondence should be sent to:
Joseph M. Hyser
Alkek Center for Metagenomic and Microbiome Research
Department of Molecular Virology and Microbiology
MS: BCM385
Baylor College of Medicine
Houston, TX, 77303
PH: 713-798-4514
FAX: 713-798-3586
Joseph.Hyser@bcm.edu

No conflicts of interest exist.

Abstract

Like many viruses, rotavirus (RV) dysregulates calcium homeostasis by elevating cytosolic calcium ([Ca^{2+}]cyt) and decreasing endoplasmic reticulum (ER) stores. While an overall, monophasic increase in [Ca^{2+}]cyt during RV infection has been shown, the nature of the RV-induced aberrant calcium signals and how they manifest over time at the single-cell level have not been characterized. Thus, we generated cell lines and human intestinal enteroids (HIEs) stably expressing cytosolic and/or ER-targeted genetically-encoded calcium indicators to characterize calcium signaling throughout RV infection by time-lapse imaging. We found that RV induces highly dynamic [Ca^{2+}]cyt signaling that manifest as hundreds of discrete [Ca^{2+}]cyt spikes, which increase during peak infection. Knockdown of nonstructural protein 4 (NSP4) attenuates the [Ca^{2+}]cyt spikes, consistent with its role in dysregulating calcium homeostasis. RV-induced [Ca^{2+}]cyt spikes were primarily from ER calcium release and were attenuated by inhibiting the store-operated calcium entry (SOCE) channel Orai1. RV-infected HIEs also exhibited prominent [Ca^{2+}]cyt spikes that were attenuated by inhibiting SOCE, underlining the relevance of these [Ca^{2+}]cyt spikes to gastrointestinal physiology and role of SOCE in RV pathophysiology. Thus, our discovery that RV increases [Ca^{2+}]cyt by dynamic Ca^{2+} signaling, establishes a new, paradigm-shifting understanding of the spatial and temporal complexity of virus-induced Ca^{2+} signaling.

Introduction

Eukaryotic signal transduction pathways employ a variety of signaling molecules to regulate cellular processes. Calcium (Ca^{2+}) is one of the most ubiquitous secondary messengers in the cell, which tightly regulates Ca^{2+} movement through the coordinated function of Ca^{2+} channels, transporters, and pumps. Since Ca^{2+} signaling modulates a wide array of cellular processes, it is not surprising that many different viruses exploit Ca^{2+} signaling to facilitate their replication, and the resulting dysregulation of Ca^{2+} signaling causes pathogenesis. Rotavirus (RV), a member of the *Reoviridae* family, is one of the first viruses shown to elevate cellular Ca^{2+} levels and has become a widely-used model system to characterize mechanisms by which viruses dysregulate host Ca^{2+} homeostasis[1]. RV is a clinically important enteric virus that causes severe diarrhea and vomiting in children, resulting in over approximately 258 million diarrhea episodes and 198,000 deaths in 2016[2]. Hyperactivation of cyclic nucleotide (*e.g.*, cAMP/cGMP) and Ca^{2+} signaling pathways is a common strategy among enteric pathogens[3]. Thus, understanding how RV exploits Ca^{2+} signaling is key to understanding and combating RV-induced diarrhea.

RV was first reported to elevate cytosolic [Ca^{2+}] by Michelangeli *et al.* (1991), which stimulated subsequent research into how RV alters cellular Ca^{2+} levels[4]. RV causes a 2-fold steady-state increase in cytosolic Ca^{2+}, which is due to increased Ca^{2+} release from the endoplasmic reticulum (ER) and increased Ca^{2+} influx through host Ca^{2+} channels in the plasma membrane (PM)[1,5]. Elevated cytosolic Ca^{2+} activates autophagy, which is critical for RV replication, and has wide-ranging consequences to

70 host cell functions, including disruption of the cytoskeleton and activation of chloride and
71 serotonin secretion to cause diarrhea and vomiting[1,5].

72 RV dysregulates Ca^{2+} homeostasis by at least two functions of its nonstructural
73 protein 4 (NSP4), a glycoprotein with multiple functions during the infection[5]. In RV-
74 infected cells, ER-localized NSP4 is a viroporin (*i.e.*, virus-encoded ion channel) that
75 releases ER Ca^{2+} and reduces ER Ca^{2+} stores causing a persistent increase in cytosolic
76 Ca^{2+} [6-8]. Using patch clamp electrophysiology, we demonstrated that the NSP4 viroporin
77 domain (aa47-90) forms a Ca^{2+}-permeable ion channel, confirming that NSP4 can
78 directly mediate loss of ER Ca^{2+} [9]. Decreased ER Ca^{2+} activates stromal interaction
79 molecule 1 (STIM1), an ER Ca^{2+} sensor, which in turn activates Ca^{2+} influx through
80 store-operated calcium entry (SOCE) channels in the PM, primarily Orai1[10]. Voltage-
81 gated Ca^{2+} channels and the sodium-calcium exchanger (NCX) have also been
82 implicated in Ca^{2+} influx in RV-infected cells[11,12]. Finally, through a mechanistically
83 distinct pathway, RV-infected cells secrete an extracellular NSP4 (eNSP4) cleavage
84 product that elicits a receptor-mediated, inositol triphosphate (IP_3)-dependent Ca^{2+}
85 signal [13,14]. eNSP4 induces diarrhea in neonatal mice, making this the first identified
86 viral enterotoxin [13,15]. At the cellular level, the eNSP4-induced Ca^{2+} signal activates
87 chloride secretion through Ca^{2+}-activated chloride channels (*e.g.*, anoctamin 1),
88 consistent with its enterotoxin activity *in vivo* [16,17]. Thus, NSP4 dysregulates Ca^{2+} by
89 both directly releasing ER Ca^{2+} and by exploiting host SOCE and agonist-induced Ca^{2+}
90 signaling pathways[1].

91 While the global dysregulation of Ca^{2+} homeostasis by RV has been well
92 characterized, many mechanistic details about RV-induced Ca^{2+} signaling remain

93 unknown. First, cell population-based studies show that RV induces a monophasic 2-
94 fold increase in cytosolic Ca^{2+} during infection[18,19], but whether individual cells manifest
95 this as a monophasic Ca^{2+} increase or a series of discrete Ca^{2+} signals remains
96 unknown. This is an important distinction because the amplitude, duration, and degree
97 of oscillation of cytosolic Ca^{2+} signals regulate downstream pathways. For example, a
98 sustained increase in cytosolic Ca^{2+} activates apoptotic programs, whereas transient or
99 oscillating Ca^{2+} signals activate proliferation and pro-survival pathways[20,21]. Second,
100 studies in single RV-infected cells have focused on times late post-infection, 7-8 hours
101 post-infection (hpi)[7,11]. Thus, it is not known whether RV dysregulates Ca^{2+} signaling
102 early in infection or how dysregulation of Ca^{2+} homeostasis progresses during the
103 infection. Finally, RV-induced depletion of ER Ca^{2+} remains controversial due to
104 conflicting data. RV decreases agonist-induced release of ER Ca^{2+} and induces STIM1
105 activation, suggesting decreased ER Ca^{2+} levels[10,22]. However, greater uptake of
106 radioactive Ca^{2+} into ER stores has also been observed[7]. As with cytosolic Ca^{2+}, ER
107 Ca^{2+} levels are dynamic; yet RV-induced changes to ER Ca^{2+} and how this relates to
108 cytosolic Ca^{2+} signaling remain incompletely characterized.
109 Addressing these gaps-in-knowledge requires the ability to measure changes in
110 cytosolic and ER Ca^{2+} with single-cell resolution over many hours. For many years,
111 technical limitations of Ca^{2+} indicator dyes (*e.g.*, photobleaching, uneven loading, and
112 dye leakage) made single-cell measurements of Ca^{2+} signaling throughout the entire RV
113 infection not feasible. However, we recently developed the use of genetically-encoded
114 calcium indicators (GECIs) for the study of Ca^{2+} signaling in virus-infected cells [23].
115 GECIs are dynamic fluorescent protein-based Ca^{2+} sensors, and variants have been

116 developed for simultaneous Ca^{2+} measurements in multiple cellular compartments (*e.g.*,
117 cytoplasm and ER) [24]. The stability and targetability of GECIs provides the spatial and
118 temporal resolution needed to perform long-term live-cell Ca^{2+} imaging such that Ca^{2+}
119 signaling can be measured throughout a RV infection. The goal of this study was to use
120 cell lines and human intestinal enteroids (HIEs) stably expressing cytoplasmic and/or
121 ER-localized GECIs to define RV-induced Ca^{2+} signaling dynamics at the single-cell
122 level, and thereby gain new mechanistic insights into how RV dysregulates Ca^{2+}
123 homeostasis.

Materials and Methods

Cells and rotaviruses. MA104 cells (African green monkey kidney cells) and HEK293T cells (ATCC CRL-3216) were cultured in high glucose DMEM supplemented with 10% fetal bovine serum (FBS) and Antibiotic/Antimycotic (Invitrogen) at 37°C in 5% CO_2. Rotavirus SA114F was produced from in-house stocks. Porcine strains OSUv and OSUa were provided as a kind gift from Dr. Lennart Svennson [25], and the human strain Ito was prepared as previously described [26]. Recombinant SA11 clone 3 expressing an mRuby3 red fluorescent protein reporter downstream of NSP3 (SA11-mRuby) was generated using a modified plasmid based reverse genetics (RG) system [27]. Briefly, the NSP4 open reading frame (ORF) in the pt7/NSP3 plasmid was replated with an ORF encoding NSP3 fused downstream to FLAG-tagged mRuby3. To promote the translation of NSP3 and mRuby3 as separate proteins, we inserted a teschovirus 2A-like stop-restart translation element between the NSP3 and FLAG-tagged mRuby3 coding sequences[28]. The SA11-mRuby virus was generated by co-transfection of BHK-T7 cells with pT7 plasmids expressing RV plus-sense RNAs along with a plasmid expressing the African swine fever virus NP868R capping enzyme from a CMV promoter. All viruses were propagated in MA104 cells in serum-free DMEM supplemented with 1 μg/mL Worthington's Trypsin, and after harvest stocks were subjected to three freeze/thaw cycles and activated with 10 μg/mL Worthington's Trypsin for 30 min at 37 °C prior to use.

Chemicals. 2-APB, KB-R7943 mesylate, BTP2 (YM 58483), and BAPTA-AM were purchased from Tocris Bioscience. Methoxyverapamil (D600), nitrotetrazolium blue

(NBT), and BCIP were purchased from Sigma-Aldrich. Synta66 and GSK7975A were purchased form Aobious. EGTA solution (0.5 M, pH 8.0) was purchased from Invitrogen.

Antibodies. To detect RV, we used rabbit anti-RV strain Alabama [29] (IF, 1:80,000; western blot, 1:3000), guinea pig anti-NSP2 [30] (IF, 1:5000), and rabbit anti-NSP4 aa120-147 [31] (western blot, 1:3000). Secondary antibodies for IF were donkey anti-rabbit AlexaFluor 568 (Invitrogen) and donkey anti-guinea pig Dylight 549 (Rockland), both at 1:2000. For western blots, we used mouse anti-GAPDH monoclonal antibody (Lifetein) (1:5000) and secondary antibodies alkaline phosphatase-conjugated goat anti-rabbit IgG or goat anti-mouse IgG (Southern Biotech) (1:2000).

Calcium indicator lentiviruses, cell lines, and enteroids. GCaMP5G (Addgene plasmid #31788), GCaMP6s (Addgene plasmid #40753), and G-CEPIA1er (Addgene plasmid #105012) were cloned into pLVX-Puro. RGECO1.2 (Addgene plasmid #45494), R-CEPIA1er (Addgene plasmid #58216), and GCaMP6s were cloned into pLVX-IRES-Hygro. Lentivirus vectors for the GECI constructs were packaged in HEK293T cells as previously described [23] or produced commercially (Cyagen Biosciences, Inc.). Production of the MA104-GCaMP5G and MA104-GCaMP5G/RCEPIAer cell lines were previously described and similar methods were used to generate MA104-RGECO1/GCEPIAer and the MA104-GCaMP6s-shRNA lines [23]. Human intestinal enteroids expressing GCaMP6s (G6S-HIEs) were created using lentivirus transduction

as described previously and grown in high Wnt3a CMGF+ with 1 µg/mL puromycin for selection[32]. Proper GECI functionality was validated by responses to 50 μM ATP.

MA104-GCaMP6s cells expressing NSP4 shRNAs. Lentivirus constructs encoding shRNA targeting SA11 gene 10 and a non-targeting scrambled shRNA negative control were generated and packaged by America Pharma Source, LLC. The NSP4-shRNA1 targets gene 10 nt50-70 (5'-GCTTACCGACCTCAATTATAC-3') and NSP4-shRNA2 targets gene 10 nt176-196 (5'-GCTACATAAAGCATCCATTCC-3'). The shRNA-expression vectors encode a blasticidin-resistance gene for drug selection. Parental MA104 cells were transduced with the shRNA-expressing constructs and at 72 hrs post-transduction the cells were passaged in the presence of 30 µg/mL blasticidin to select for stably transduced cells. These three cell lines were then transduced with GCaMP6s GECI (in pLVX-IRES-Hygro) and passaged with 50 μg/mL hygromycin B and 30 μg/mL blasticidin to select for co-expression of GCaMP6s and the shRNA.

Establishment of HIE cultures. Three-dimensional human intestinal enteroid (HIE) cultures were generated from crypts isolated from adult patients undergoing bariatric surgery as previously described[26,33]. These established cultures were obtained at Baylor College of Medicine through the Texas Medical Center Digestive Diseases Center Gastrointestinal Experimental Model Systems Core. For these studies, jejunum HIEs from patient J3 were used. Complete media with and without growth factors (CMGF+ and CMGF-, respectively), differentiation media, and high Wnt3a CMGF+ (hW-CMGF+) were prepared as previously described[26,33,34]. Fluorobrite DMEM supplemented with

15mM HEPES, 1X sodium pyruvate,1X Glutamax, and 1X non-essential amino acids (Invitrogen) was used for fluorescence Ca^{2+} imaging (FB-Plus). An FB-Plus-based differentiation medium (FB-Diff) consisted of FB-Plus with the same added components as differentiation media, but without Noggin. HIEs were grown in phenol red-free, growth factor-reduced Matrigel (Corning). G6S-jHIE monolayers were prepared from three-dimensional cultures and seeded into optical-bottom 10-well Cellview chamber slides coated with dilute collagen IV (Sigma) as described previously[35,36]. After 24 hr in CMGF+ and 10 μM Y-27632 Rock inhibitor, differentiation medium was used and changed every day for 4-5 days.

Microscopy and image analysis. To image viroplasms, we used a GE Healthcare DeltaVision LIVE High Resolution Deconvolution with an Olympus IX-71 base and illumination provided by a xenon lamp. Images were captured with Plan Apo 60X Oil DIC objective and a pco.edge sCMOS camera. Images were acquired and deconvolved using SoftWoRx software and further analyzed with Fiji (ImageJ).

For calcium imaging, MA104 cells and HIEs were imaged with a widefield epifluorescence Nikon TiE inverted microscope using a SPECTRAX LED light source (Lumencor) and either a 20x Plan Fluor (NA 0.45) phase contrast or a 20X Plan Apo (NA 0.75) differential interference contrast (DIC) objective. Fluorescence and transmitted light images were recorded using an ORCA-Flash 4.0 sCMOS camera (Hamamatsu), and Nikon Elements Advanced Research v4.5 software was used for multipoint position selection, data acquisition, and image analysis.

Images were read-noise subtracted using an average of 10 no-light acquisitions of the camera. Single cells were selected as Regions of Interest (ROI) and fluorescence intensity measured for the experiment. 3D HIE's fluorescence was measured individually using threshold analysis adjusted to select each enteroid with the Fill Holes algorithm included. Enteroids that moved out of the field of view or could not be separated from adjacent enteroids were removed from analysis. The fluorescence intensity of whole field-of-view was measured for HIE monolayers.

Fluorescence intensity values were exported to Microsoft Excel and normalized to the baseline fluorescence. The number and magnitude of Ca^{2+} spikes were calculated by subtracting each normalized fluorescence measurement from the previous measurement to determine the change in GECI fluorescence (ΔF) between each timepoint. Ca^{2+} signals with a ΔF magnitude of > 5% were counted as Ca^{2+} spikes.

Calcium imaging. *MA104-GECI cells.* Confluent monolayers of MA104-GECI cells in 8-well chamber slides (ibidi) were mock- or RV-infected in FBS-free media for 1 hr at the indicated multiplicity of infection (MOI). Then the inoculum was removed and replaced with FB-Plus, and for appropriate studies, with DMSO or drugs at indicated concentrations. The slide was mounted into an Okolab stage-top incubation chamber equilibrated to 37°C with a humidified 5% CO_2 atmosphere. For each experiment, 3-5 positions per well were selected and imaged every 1 minute for ~18-20 hrs.

GECI HIEs. To test Ca^{2+} response, 3D G6S-jHIEs were suspended in 25% Matrigel diluted in FB-Diff media and seeded into optical-bottom 10-well Cellview chamber slides (Greiner bio-one) thinly coated with Matrigel. After baseline imaging using the stage-top

incubator, 200μM carbachol in FB-Diff or FB-Diff alone was added to the well and imaging continued for 1 hour with 6-10 enteroids imaged every 10 s.

For RV infection in 3D HIEs, the jHIEs were split and grown in hW-CMGF+ for 2 days followed by differentiation medium for 1 day. G6S-jHIEs were gently washed using ice cold 1XPBS and resuspended in inoculum of 50μL MA104 cell lysate or RV (strain Ito) diluted with 150 μL CMGF- and incubated for 1 hr. Then HIEs were washed, resuspended in 25% Matrigel diluted in FB-Diff (with DMSO or 2-APB in indicated experiments) and pipetted onto 8-well chamber slides (Matek) pre-coated with Matrigel. Imaging positions were chosen so that between 20-50 enteroids were selected per experimental condition. Enteroids were imaged using the stage-top incubator with transmitted light and GFP fluorescence every 2-3 minutes for ~18 hrs.

For RV infection in monolayers, G6S-jHIE monolayers were washed once with CMGF- and treated with an inoculum of 50μL CMGF- plus 30μL MA104 cell lysate or RV (strain Ito) and incubated for 2 hr. Then inoculum was removed, and monolayers were washed once with FB-Diff before adding FB-Diff with DMSO or 2-APB. Monolayers were transferred to the stage-top incubator for imaging with 4 fields of view chosen per well, and GFP fluorescence was measured every minute for ~18 hrs.

Store-operated calcium entry assay. G6S-jHIE monolayers after 4 days in differentiation media were washed and incubated in 0 mM Ca^{2+} ($0Ca^{2+}$) Ringers solution (160 mM NaCl, 4.5 mM KCl, 1 mM $MgCl_2$, 10 mM HEPES, pH=7.4). Endoplasmic reticulum Ca^{2+} stores were depleted by incubating cells with 500 nM thapsigargin in $0Ca^{2+}$ with either 50 μM 2-APB or DMSO as a vehicle control. SOCE was measured

using live-cell fluorescence imaging of the increase in GFP fluorescence after the addition of normal Ringers to bring the total Ca^{2+} concentration to 2 mM.

Western blot analysis. RV proteins were detected by immunoblot analysis as previously described, with the following modifications[31]. Cells were lysed using a 1X RIPA buffer solution [10 mM Tris-HCL pH 8.0, 1 mM EDTA, 1% Triton X-100, 0.1% sodium deoxycholate, 0.1% SDS, 140 mM NaCl, and 1 tablet complete mini protease inhibitor (Roche)] and passed through a Qiashredder (Qiagen). Samples were boiled for 10 min at 100°C in SDS-PAGE sample buffer and separated on Tris-glycine 4-20% SDS-PAGE gels (BioRad). Detected protein bands for each blot were quantified using ImageJ software for gel densitometry measurements of NSP4:GAPDH.

Immunofluorescence. MA104 cells and HIEs were fixed using the Cytofix/Cytoperm kit (BD Biosciences) according to manufacturer instructions. Primary antibodies were diluted in 1X Perm/Wash overnight at 4°C. The next day, the cells were washed three times with 1X Perm/Wash solution and then incubated with corresponding secondary antibodies for 1 hr at room temperature. Nuclei were stained with NucBlue Fixed Cell Stain (Life Technologies) for 5 min at room temperature and washed with 1X PBS for imaging.

Plaque assays. Plaque assays were performed as described previously with the following modifications [37]. Briefly, MA104 cells or the MA104-shRNA expressing cells were seeded and grown to confluency in 6 wells plates. Wells were infected at 10-fold

dilutions in duplicate for 1 hr and media replaced with an overlay of 1.2% Avicel in serum-free DMEM supplemented with DEAE dextran, and 1µg/mL Worthington's Trypsin, and, for indicated experiments, DMSO vehicle or SOCE drugs[38]. The cells were incubated at 37°C/5% CO_2 for 48-72 hrs before overlay was removed and cells stained with crystal violet to count plaques.

RNA extraction, reverse transcription, and quantitative PCR. Total RNA was extracted from HIEs wells (in hW-CMGF+ or differentiation media for 4 days) or MA104 cells grown to confluency in a 6-well plate using TRIzol reagent (Ambion). Total RNA was treated with Turbo DNase I (Ambion) and cDNA was generated from 250 ng RNA using the SensiFAST cDNA synthesis kit (Bioline). Quantitative PCR was performed using Fast SYBR Green (Life Technologies) with primers designed using NCBI Primer-Blast (Table 1) and using a QuantStudio real time thermocycler (Applied Biosciences). Target genes were normalized to the housekeeping gene ribosomal subunit 18s and relative expression was calculated using the ddCT method.

Statistical analysis. Biostatistical analyses were performed using GraphPad Prism (version 8.1) with results presented as mean ± standard deviation. Comparisons used an unpaired Student's t-test, the nonparametric Mann-Whitney test, or a One-way Analysis of Variance (ANOVA) with Tukey's post hoc multiple comparisons test where appropriate. Differences were considered statistically significant for $p < 0.05$. All authors had access to the study data, reviewed, and approved the final manuscript.

306 **Results**

307 Previous studies have shown that RV significantly increases cytosolic Ca^{2+} over
308 several hours during the peak of RV replication[18,39]; however, the kinetics of this
309 increase and whether it is a monophasic increases or manifests as discrete Ca^{2+}
310 transients are not known. To address these questions, we developed a series of cell
311 lines stably expressing GECIs and used these cell lines to perform live-cell Ca^{2+}
312 imaging over the course of a RV infection[23]. For the long-term imaging experiments,
313 MA104 cells stably expressing cytosolic GCaMP5G (MA104-GCaMP5G) were seeded
314 into chamber slides and either mock- or RV-infected with strain SA114F (MOI 10), and
315 GCaMP5G fluorescence imaged for ~18 hr (2-20 hpi) (Fig. 1). Mock-infected cells
316 maintained a low fluorescence throughout the time course (Fig. 1A, upper panels),
317 whereas RV-infected cells exhibited strongly increased fluorescence, indicating
318 elevated Ca^{2+} levels (Fig. 1A, lower panels and Supplementary Video 1 online). Since
319 GECIs use an engineered calmodulin to sense Ca^{2+}, overexpression of GCaMP5G
320 could act as a Ca^{2+} buffer and alter the kinetics of RV replication. To assess whether
321 the MA104-GCaMP5G cells exhibited altered RV infection/protein synthesis, we
322 analyzed NSP4 expression in parental MA104 cells and the MA104-GCaMP5G cells
323 infected with SA114F (MOI 10) from 3-8 hpi by western blot (Fig. 1B). NSP4 expression
324 was similar in both parental and GCaMP5G-expressing cells, indicating that stable
325 GCaMP5G expression does not interfere with RV infection.

326 Next, we measured changes in cytosolic Ca^{2+} by determining the relative
327 GCaMP5G fluorescence (F/F_0) for the whole field-of-view (FOV) (~455 μm^2) for three
328 replicate infections and time lapse images were acquired once per minute (Fig. 1C).

Mock-infected cells maintained low Ca^{2+} levels with few transient and low amplitude Ca^{2+} signals (Fig. 1C, black and grey lines). In RV-infected cells, the steady-state Ca^{2+} levels began to increase at ~6 hpi, and we observed many large amplitude, transient Ca^{2+} signals that occurred concomitantly with the steady-state elevation in cytosolic Ca^{2+} levels (Fig. 1C, arrow). Further, at 6-8 hpi the RV-infected cells had more low and moderate amplitude Ca^{2+} signals than mock-infected cells (Fig. 1D, arrows), which occurred during the initial increase in steady-state Ca^{2+} levels. A more detailed examination of the Ca^{2+} signaling over a period of 5 mins at 480 minutes post-infection (~8 hpi) shows that the increase in cytosolic Ca^{2+} manifests as discrete and dynamic Ca^{2+} fluxes from individual or small groups of cells (Fig. 1E). The dynamic changes are exemplified by the two areas outlined (Fig. 1E, magenta or yellow box), showing substantial changes over the 5 min period. To compare our GECI-based Ca^{2+} imaging of RV-induced Ca^{2+} signaling to previous cell population-based studies, we determined the average GCaMP5G fluorescence from 18-19 hpi (Fig. 1F) and the slope of the fluorescence increase from 8-18 hpi (Fig. 1G). We found a similar ~2-fold increase in $[Ca^{2+}]c$ and a rate of Ca^{2+} increase consistent with that found in studies using Ca^{2+} indicator dyes [12,18,19]. Thus, the MA104-GCaMP5G cells exhibit the well-characterized hallmarks of RV-induced Ca^{2+} dysregulation but have greater spatial and temporal resolution to study Ca^{2+} in RV-infected cells. This has revealed a new dimension of the RV-induced Ca^{2+} signaling, in that the cytosolic Ca^{2+} increase manifests through highly dynamic and discrete Ca^{2+} signaling events, which had not been previously observed.

RV-induces dynamic Ca^{2+} signaling

352 Our long-term Ca^{2+} imaging approach using MA104-GCaMP5G cells had
353 sufficient resolution to enable analysis of Ca^{2+} signaling at the single-cell level over the
354 course of the RV infection. Three representative traces from mock- or RV-infected cells
355 (MOI 10, imaged once per minute) show that while individual cells display unique
356 characteristics of Ca^{2+} signaling, they all exhibit similar patterns of Ca^{2+} signaling (Fig.
357 2A). Mock-infected cells maintain low cytosolic Ca^{2+} with few low amplitude Ca^{2+} signals
358 (Fig. 2A, black lines), but RV-infected cells display a large number of large amplitude
359 Ca^{2+} transients, as well as an overall increase in cytosolic Ca^{2+} (Fig. 2A, red lines).
360 These Ca^{2+} transients were the most prominent Ca^{2+} signal during the infection and
361 were infrequently detected in mock-infected cells. Finally, as RV is a lytic virus, we
362 observed clear evidence of cell lysis late in infection, but this was associated with a loss
363 of GCaMP5G signal and dynamics because the sensor diffused away from the ruptured
364 cells (see Supplementary Video 1 online). We sought to determine a threshold to define
365 these "Ca^{2+} spikes" so that we could measure the number and amplitude of these Ca^{2+}
366 signals. To define a "Ca^{2+} spike", we set a cutoff for the change in GCaMP5G
367 fluorescence between two measurements to be greater than 5% ($\Delta F > 5\%$). The mean
368 Ca^{2+} transient amplitude of mock-infected cells was 0.3% ($\pm$ 0.5% standard deviation)
369 (data not shown; see Fig. 2D for a subset of this data). Thus the $\Delta F > 5\%$ cutoff is more
370 than 3 standard deviations above the mean, which establishes a stringent threshold for
371 quantitating Ca^{2+} spikes. Next, we determined the change in fluorescence between
372 each data point and found that the majority of Ca^{2+} spikes were captured in 1 image
373 (Fig. 2B). This simple method enabled detection of Ca^{2+} spikes with approximately 80%
374 accuracy; however, it results in a 20% under-estimation of Ca^{2+} spikes, which were

375 captured in 2-3 images (Fig. 2C, black dots). Nevertheless, using this method of Ca^{2+}
376 spike analysis, we found that RV significantly increases the number of Ca^{2+} spikes per
377 cell (Fig. C). We then determined the amplitude for the top 150 Ca^{2+} spikes per
378 representative cell and found that while the amplitude was highly variable between RV-
379 infected cells, these signals were significantly greater than mock-inoculated cells (Fig.
380 2D). Finally, we compared the RV-induced Ca^{2+} spikes to the Ca^{2+} response induced by
381 10 μM ATP (Fig. 2E). As expected, ATP induced a strong Ca^{2+} flux that was similar to
382 the amplitude of Ca^{2+} spikes induced during RV infection. Although the ATP-induced
383 response was significantly greater than the RV-induced Ca^{2+} spikes, it is important to
384 note that the amplitude of the ATP-induced signals represent the peak of the Ca^{2+}
385 response, whereas it is not possible to know how many of the RV-induced Ca^{2+} spikes
386 were captured at the peak of the signal. Thus, at the individual cell level, a high MOI RV
387 infection induces up to hundreds of discrete and high amplitude Ca^{2+} signaling events.
388 Next, we determined how these RV-induced Ca^{2+} signals differ with respect to
389 different infectious doses. We infected MA104-GCaMP5G cells with SA114F or with a
390 recombinant SA11 cl. 3 expressing mRuby from the NSP3 gene (SA11cl3-mRuby) [28].
391 Cells were infected at MOI of 10, 1, or 0.1, and we performed time-lapse Ca^{2+} imaging
392 and single-cell analysis of the resulting Ca^{2+} signaling. Infection of cells with native
393 SA114F at different MOIs showed the expected infectious dose-dependent increase in
394 the number of RV-positive cells (Fig. 3A). Similarly, the SA11cl3-mRuby-infected cells
395 exhibited an infectious dose-dependent increase in the number of RFP-positive cells at
396 7 hpi (Fig. 3B), as well as an increase in RFP intensity from 7 hpi to 10 hpi (Fig. 3C).
397 Representative single-cell Ca^{2+} traces for SA114F-infected cells show similar dynamic

398 increases in cytosolic Ca^{2+} spikes as before, but cells infected with lower MOIs of 1 and
399 0.1 exhibited a later onset of the Ca^{2+} signaling and generally fewer and lower
400 amplitude Ca^{2+} spikes (Fig. 3D). The virus dose-dependent differences in the Ca^{2+}
401 signaling are clearly demonstrated by the time-lapse imaging at 6-7 hpi, which are
402 superimposed onto the immunofluorescence images to detect RV-positive cells
403 (Supplementary Video 2 online). In a more detailed examination of cytosolic Ca^{2+} in RV-
404 infected cells, we used a higher image acquisition frequency (1 image/1.5 sec) and
405 again observed active and dynamic Ca^{2+} signaling. While virtually every cell exhibited
406 multiple Ca^{2+} transients over the course of 10 mins, the Ca^{2+} spike frequency and
407 amplitude were variable from cell-to-cell (Supplemental Figure 1 & Supplementary
408 Video 3 online). We quantitated the number of Ca^{2+} spikes throughout the infection and
409 found a dose-dependent decrease in the number of spikes per cell (Fig. 3F) for lower
410 MOI infections. A similar phenotype was observed in cells infected with SA11cl3-
411 mRuby, but in this case the mRuby expression enabled us to measure both Ca^{2+}
412 signaling and RV protein expression (Fig. 3E & Supplementary Video 4 online). We
413 again observed that for lower MOI infections the onset of Ca^{2+} signaling was later, and
414 the Ca^{2+} spike number and amplitude were generally lower. Further, onset of the Ca^{2+}
415 signaling corresponded to the detection of mRuby from the NSP3 gene. Quantitation of
416 the number of Ca^{2+} spikes per cell for SA11cl3-mRuby infections also showed a dose-
417 dependent decrease with infectious dose (Fig. 3G). Thus, the number and amplitude of
418 these Ca^{2+} signaling events are related to both the infectious dose of RV and onset of
419 RV protein synthesis.

420 Next, we sought to characterize the Ca^{2+} signaling phenotype of different RV
421 strains that infect humans or other animals. We compared the Ca^{2+} signaling in MA104-
422 GCaMP5G cells infected at MOI 1 with simian strain SA114F to that of human strain Ito.
423 Immunofluorescence staining of Ito-infected cells (Fig. 4A) showed a similar number of
424 infected cells as that for SA114F infected above (Fig. 3A). As above, we quantitated the
425 number of Ca^{2+} spikes per cell and found that both SA114F and Ito induced a significant
426 increase in Ca^{2+} spikes compared to mock-infected cells (Fig. 4B). These findings
427 demonstrate that the dynamic Ca^{2+} signaling phenotype is not exclusively a feature of
428 animal RV strains. Further, we investigated the attenuated and virulent porcine OSU
429 strains (OSUa and OSUv). Mutations in the OSUa NSP4 protein are associated with
430 reduced elevation in cytosolic Ca^{2+} levels in recombinant NSP4-expressing Sf9 cells [40],
431 but the Ca^{2+} signaling phenotype of these two viruses had not been studied in the
432 context of an infection. Immunofluorescence of OSUa and OSUv-infected MA104 cells
433 at MOI 1 show a similar number of infected cells (Fig. 4A). However, while both OSUa
434 and OSUv significantly increase the number of Ca^{2+} spikes, the number of Ca^{2+} spikes
435 from OSUa-infected cells is significantly less than that of those infected with OSUv (Fig.
436 4B & Supplementary Video 5 online). To characterize this difference further, we
437 examined single-cell traces for OSUa-and OSUv-infected cells (Fig. 4C). We found that
438 OSUa-infected cells initially induced a low-amplitude monophasic increase in cytosolic
439 Ca^{2+} levels (Fig. 4C, black arrows), with the onset of the dynamic Ca^{2+} spikes occurring
440 several hours later (Fig. 4C, purple traces). In contrast, OSUv infection induced a much
441 earlier onset of the dynamic Ca^{2+} spiking, which explains the higher number of Ca^{2+}
442 spikes per cell (Fig. 4C, blue traces). Interestingly, OSUv may also induce an early, low-

amplitude increase in cytosolic Ca^{2+} in addition to the dynamic Ca^{2+} spikes, but the high number of Ca^{2+} spikes makes it difficult to clearly ascertain this in all but a few cells (Fig. 4C, red arrow). Together, these data demonstrate that the dynamic Ca^{2+} signaling phenotype is a commonly feature among RV strains and potentially related to NSP4's role in dysregulating host Ca^{2+} homeostasis and virus virulence.

Ca^{2+} signaling dynamics are dependent on NSP4 expression

RV NSP4 is the primary mediator of elevated Ca^{2+} levels during RV infection. The differences in Ca^{2+} signaling by OSUa and OSUv observed in Fig. 4 suggest that NSP4 expression is important for the induction of the dynamic Ca^{2+} signaling during infection[1]. To test the role of NSP4 in these Ca^{2+} signals, we made two GCaMP6s cell lines, each stably expressing a different short-hairpin RNA that targets SA11 NSP4 (NSP4 shRNA1 and NSP4 shRNA2), and a third GCaMP6s cell line stably expressing a non-targeted scrambled shRNA. Cells were infected with SA114F (MOI 0.01), and we found that cells expressing NSP4-targeted shRNAs exhibited knockdown of NSP4 protein levels (Fig. 5A). We normalized NSP4 expression to GAPDH and found ~40% knockdown in cells expressing NSP4 shRNA1 and ~85% knockdown in cells expressing NSP4 shRNA2 (Fig. 5B), which correlated with reduced RV plaque size (Fig. 5C). To examine the Ca^{2+} signaling phenotype, we then infected the cells with SA114F (MOI 0.1) and used live-cell imaging to measure Ca^{2+} signaling from ~2-18 hpi. The scrambled shRNA-expressing cells exhibited a similar degree of dynamic Ca^{2+} signaling as observed in parental MA104 cells (Fig. 5D, red traces), whereas knockdown of NSP4 substantially decreased the degree of Ca^{2+} signaling observed (Fig. 5D, blue traces).

Upon quantitation, we found the number of Ca^{2+} spikes was significantly reduced in the NSP4 knockdown cells (Fig. 5E). Together, these data show that NSP4 is responsible for inducing these dynamic Ca^{2+} signals during infection.

RV-induced Ca^{2+} spikes require extracellular and ER Ca^{2+} pools

NSP4 elevates cytosolic Ca^{2+} by activating both uptake of extracellular Ca^{2+} and release of ER Ca^{2+} pools. Thus, we next sought to characterize which pools of Ca^{2+} were critical for supporting the RV-induced Ca^{2+} spikes. First, we tested whether extracellular Ca^{2+} influenced the RV-induced Ca^{2+} spikes. We infected MA104-GCaMP5G cells with SA114F (MOI 1), and at 1 HPI replaced the media with either normal media containing 2 mM Ca^{2+}, media without Ca^{2+} (supplemented with 1.8 mM EDTA), or media supplemented with Ca^{2+} for a 10 mM final concentration. The imaging data shows that decreasing extracellular Ca^{2+} strongly reduced the number and duration of Ca^{2+} signaling (Fig. 6A, light blue), whereas cells maintained in media with 2 mM or 10 mM extracellular Ca^{2+} showed increased dynamic Ca^{2+} signaling (Fig. 6A, red & purple). As before, mock-infected cells in each condition exhibited little to no induction of the Ca^{2+} signaling (Fig. 6A, black lines). Quantitation of the number of Ca^{2+} spikes showed that RV-infected cells in low extracellular Ca^{2+} exhibited significantly fewer Ca^{2+} spikes than that of cells in normal extracellular Ca^{2+}, but this was still greater than that of mock-infected cells (Fig. 6B). Interestingly, there was no difference in the number of Ca^{2+} spikes per cell when maintained in 2 mM versus 10 mM Ca^{2+} media (Fig. 6B). However, the traces indicated that the magnitude of the Ca^{2+} spikes were greater in high Ca^{2+} media. Thus, we then determined the Ca^{2+} spike amplitude for the top 50

489 Ca^{2+} spikes, and while this was highly variable from cell-to-cell, this trended to be
490 greater with higher extracellular Ca^{2+} concentrations (Fig. 6C). Together, these data
491 indicate that normal extracellular Ca^{2+} levels are critical for the RV-induced Ca^{2+} spikes,
492 which could occur both through discrete Ca^{2+} influx events through the plasma
493 membrane, and by influx of extracellular Ca^{2+} serving to maintain ER Ca^{2+} stores to
494 feed ER Ca^{2+} release events.

495 The ER is the major intracellular Ca^{2+} store, and RV NSP4 has been shown to
496 decrease ER Ca^{2+} levels both during infection and by recombinant expression [6,7].
497 However, controversy remains about whether RV causes a sustained depletion in ER
498 Ca^{2+} [22]. Thus to directly characterize the change in ER Ca^{2+} during RV infection, and
499 determine how this relates to the dynamic cytosolic Ca^{2+} spikes, we generated an
500 MA104 cell line co-expressing R-GECO1.2 and GCEPIAer (MA104-
501 RGECO1/GCEPIAer), in which R-GECO1.2 is a red fluorescent cytoplasmic GECI and
502 GCEPIAer is a green fluorescent ER-targeted GECI [24,41]. As above, infection with
503 SA114F (MOI 1) induced highly dynamic cytoplasmic Ca^{2+} signaling by ~8 hpi, as
504 illustrated in two representative single-cell traces (Fig. 7A-B, red traces; Supplementary
505 Video 6 online). Concomitant with the onset of the cytoplasmic Ca^{2+} signaling was an
506 equally dynamic decrease of ER Ca^{2+} that persisted throughout the rest of the infection
507 (Fig. 7A-B, green traces). We examined the relationship between the cytoplasmic Ca^{2+}
508 spikes and ER Ca^{2+} troughs more closely from 8-12 hpi (Fig. 7B), which was during the
509 onset of these signaling events. First, we found that the onset of Ca^{2+} signals in the
510 cytoplasm coincided with the ER Ca^{2+} release events (Fig. 7B, black arrowheads). The
511 persistent decrease in ER Ca^{2+} observed was driven primarily by this continuous

512 signaling, such that the ER Ca^{2+} level never recovered to the baseline level (Fig. 7A).
513 Interestingly, a small number of ER Ca^{2+} troughs were not associated with a
514 concomitant cytoplasmic Ca^{2+} spike (Fig. 7B, magenta arrowheads). Over the course of
515 the long-term imaging experiment, mock-infected cells exhibited a 10% decrease in
516 GCEPIAer fluorescence, but RV-infected cell had a 30% decrease (Fig. 7C), which
517 occurred rapidly from 8-12 HPI (Fig. 7A). The decrease in GCEPIAer in mock-infected
518 cells likely represents modest photobleaching of GCEPIAer over the imaging
519 experiment.

520 During these studies, we observed that the ER-localized GCEPIAer protein is
521 also redistributed during the RV infection, which is illustrated for a single cell in Fig. 7D-
522 E and Supplementary Video 7. At the beginning of the imaging run (3 hpi), the
523 GCEPIAer signal was high and localized throughout the ER in a reticular pattern (Fig.
524 7D-E, left) but by 10.7 HPI, RV-induced Ca^{2+} signaling had decreased GCEPIAer
525 fluorescence to its nadir (Fig. 7D-E, middle), representing a substantial decrease in ER
526 Ca^{2+}. Approximately 2 hrs after the initial decrease in ER Ca^{2+}, the GCEPIAer began
527 accumulating into circular domains that are likely the ER-derived compartment
528 surrounding viroplasms (Fig. 7D-E, right). These structures become more pronounced
529 through the late stages of the infection, ~13 hpi (Fig. 7D, arrows). While the absolute
530 onset of the ER Ca^{2+} release events was variable, the formation of viroplasm-
531 associated membranes subsequent to the decrease in ER Ca^{2+} was a consistent
532 pattern among RV-infected cells (Supplementary Video 7 online). Using immunostaining
533 and deconvolution microscopy, we confirmed that the structures are viroplasms
534 because they contain RV nonstructural protein 2 (NSP2), a major component of

535 viroplasms (Fig. 7F). Interestingly, during late stages of infection when viroplasms are
536 forming, we detected a modest recovery in ER Ca^{2+} from its nadir (Fig. 7E), which may
537 reflect the increased $^{45}Ca^{2+}$ uptake previously observed[22].
538
539 **SOCE blockers reduce RV-induced Ca^{2+} spikes**
540 Since removing extracellular Ca^{2+} diminishes the RV-induced Ca^{2+} spikes (Fig.
541 6), cellular Ca^{2+} influx pathways are critical for these Ca^{2+} signals. Several host Ca^{2+}
542 channels have been implicated in mediating Ca^{2+} entry into RV-infected cells, including
543 SOCE channels, voltage-activated Ca^{2+} channels (VACC), and the sodium-calcium
544 exchanger (NCX) [10-12]. To determine which pathway(s) were important for the dynamic
545 Ca^{2+} spikes in RV infection, we used pharmacological blockers targeting each pathway
546 (2-APB for SOCE; D600 for VACC; KB-R7943 for NCX). MA104-GCaMP5G cells were
547 infected with SA114F (MOI 1), and then treated with different concentrations of the
548 blockers at 1 hpi and imaged to measure GCaMP5G fluorescence. None of the blockers
549 exhibited cytotoxic effects to uninfected cells (data not shown). Cells treated with DMSO
550 as a vehicle control exhibited the dynamic Ca^{2+} spikes as above (Fig. 8A, red trace). In
551 contrast, cells treated with the SOCE blocker 2-APB exhibited a dose-dependent
552 decrease in both the number and amplitude of the Ca^{2+} signaling (Fig. 8A, green
553 traces). Traces from cells treated with the NCX blocker KB-R7943 showed a modest
554 decrease in Ca^{2+} signaling (Fig. 8A, brown traces), whereas there was no difference in
555 Ca^{2+} signaling for cells treated with D600 (data not shown). We also noted that RV-
556 infected cells treated with 10 μM KB-R7943 underwent cell death more frequently than
557 any other treatment, which was marked by a rapid increase in cytosolic Ca^{2+} and then

558 lysis (Fig. 8A, arrowhead); however, cell death was not observed in uninfected cells
559 treated with KB-R7943 (data not shown). We quantitated the number of Ca^{2+} spikes per
560 cell, which showed a significant, dose-dependent decrease in the number of Ca^{2+}
561 spikes for both 2-APB-treated (Fig. 8B, green) and, to a lesser extent, KB-R7943-
562 treated (Fig. 8B, brown) cells, but no difference for D600-treated cells (Fig. 8B, blue).
563 We further investigated the effects of 2-APB and KB-R7934 by examining the amplitude
564 of the largest 50 Ca^{2+} spikes of three representative cells shown in Fig. 8C-D.
565 Treatment with 2-APB showed a dose-dependent decrease in the Ca^{2+} spike amplitude
566 (Fig. 8C), consistent with the single-cell traces, but treatment with KB-R7943 showed no
567 difference in spike amplitude.

568 Since elevated cytosolic Ca^{2+} is critical for RV replication, we examined RV
569 protein levels by immunoblot to determine whether 2-APB or KB-R7943 reduced the
570 Ca^{2+} signaling by merely blocking RV or NSP4 protein synthesis or protein stability[42].
571 Immunoblot detection with an anti-RV antisera (Fig. 8E) or an anti-NSP4 specific
572 antisera (Fig. 8F) show that none of the Ca^{2+} channel blockers caused substantial
573 decrease in RV or NSP4 protein levels. However, we observed that 2-APB treatment
574 significantly increased the 20 kDa unglycosylated NSP4 band (Fig. 8F) by gel
575 densitometry analysis (Fig. 8G).

576 Overall the SOCE blocker 2-APB was the most potent inhibitor of the RV-induced
577 dynamic Ca^{2+} signaling, so we examined the effect of other SOCE blockers that also
578 target the Orai1 Ca^{2+} channel. MA104 cells express the Orai1 Ca^{2+} channel and the
579 STIM1 and STIM2 ER Ca^{2+} sensors, which are the core machinery for the SOCE
580 pathway (Fig. 9A). While MA104 cells also express the Orai3 Ca^{2+} channel, this isoform

581 is not activated by ER Ca^{2+} store depletion but arachidonic acid and leukotrienes [43]. We
582 tested four SOCE blockers (2-APB, BTP2, Synta66, and GSK7975A) for the ability to
583 block thapsigargin-induced SOCE and found that all of them showed a similar inhibition
584 of Ca^{2+} entry after ER store depletion (Fig. 9B). Thus, we treated SA114F-infected
585 MA104-GCaMP5G cells with each of these blockers at ~1 hpi and performed Ca^{2+}
586 imaging to measure the RV-induced Ca^{2+} spikes (Fig. 9C-D). Representative single-cell
587 traces illustrate that all the SOCE blockers inhibited the RV-induced dynamic Ca^{2+}
588 signaling (Fig. 9C) and significantly inhibited the number of Ca^{2+} spikes per cell (Fig.
589 9D). The blockers displayed varying degrees of potency but 2-APB and BTP2 treatment
590 caused the greatest decrease in RV-induced Ca^{2+} signaling (Supplementary Video 8
591 online). Further, we found that treatment with the SOCE blockers significantly reduced
592 RV yield from MA104 cells (Fig. 9E), which is consistent with the importance of elevated
593 cytosolic Ca^{2+} for RV replication[29]. As with the other Ca^{2+} channel blockers, we
594 examined whether the SOCE blockers affected viral protein levels by immunoblot. As
595 above, we found that 2-APB treatment increased the abundance of the 20 kDa
596 unglycosylated NSP4 band (NSP4-20), and Synta66 treatment also caused a modest
597 increase in NSP4-20 (Fig. 9F). In contrast to the other SOCE blockers, BTP2 treatment
598 caused an overall decrease in RV proteins, which correlates with the strong
599 suppression of RV-induced Ca^{2+} signaling during the infection (Fig. 9D & 9F). Together,
600 these data support the previous observation that shRNA knockdown of the Ca^{2+} sensor
601 STIM1 reduces RV replication, and further show that Ca^{2+} influx *via* SOCE channels is
602 critical for RV-induced Ca^{2+} signaling and replication[10].
603

Human intestinal enteroid characterization of RV-induced Ca^{2+} signaling

Although MA104 cells provide a robust model for RV replication and form a single epithelial sheet ideal for microscopy studies, they are neither of human nor of intestinal cell origin. Human intestinal enteroids (HIEs) have been developed as a model *in vitro* system of the epithelial cells of the small intestine, and support RV infection and replication, particularly for human RV strains [26,44]. HIEs are grown in "mini-gut" three-dimensional (3D) cultures from human intestinal stem cells and are non-transformed cells, which make them a biologically relevant system to study the GI epithelium[45]. Thus, we sought to determine if the dynamic cytosolic Ca^{2+} signaling observed in MA104 cells were also observed in HIEs with RV infection.

We created jejunum HIEs stably expressing the green cytoplasmic GECI GCaMP6s (jHIE-GCaMP6s) using lentivirus transduction. To test the response of GCaMP6s to cytoplasmic Ca^{2+} in the enteroids, we treated 3D jHIE-GCaMP6s stabilized in a diluted Matrigel, with carbachol, a known Ca^{2+} agonist. Carbachol treatment of jHIE-GCaMP6s significantly increased GCaMP6s fluorescence 200-300% over the mock-treated jHIE-GCaMP6s (Fig. 10A-C). Thus, jHIE-GCaMP6s enteroids functionally report changes in cytoplasmic Ca^{2+} and can be used to examine RV-induced Ca^{2+} signaling.

We next tested if 3D jHIE-GCaMP6s enteroids would exhibit similar Ca^{2+} dynamics during RV infection as observed in MA104-GCaMP5G cells. jHIE-GCaMP6s enteroids were mock- or RV-infected with the human RV strain Ito, seeded into chamber slides in diluted Matrigel, and imaged every 2-3 minutes for phase contrast and GCaMP6s fluorescence throughout the RV infection (~16 hrs). At 24 hpi, the HIEs were fixed and immunostained for RV antigens to confirm successful infection, which is

627 evident by both infected cells within the HIEs as well as strong positive staining of the
628 dead cells sloughed from the HIEs (Fig. 10D). Examination of the Ca^{2+} signaling
629 showed little Ca^{2+} signaling activity in the mock-infected jHIE-GCaMP6s enteroids, but
630 RV-infected enteroids exhibited significantly increased Ca^{2+} dynamics, as illustrated in
631 representative traces from three mock- or RV-infected HIEs (Fig. 10E and
632 Supplementary Video 9 online). Similar to the Ca^{2+} signaling observed in MA104 cells,
633 initially there were no or only modest changes in cytosolic Ca^{2+}, and the onset of strong
634 and dynamic Ca^{2+} signals occurred ~8-10 HPI. For HIEs it was not possible to
635 accurately measure Ca^{2+} signaling at the single-cell level. We were able to track and
636 measure Ca^{2+} signaling over the entire jHIE-GCaMP6s enteroid and quantify these
637 changes as Ca^{2+} spikes/enteroid. We found that RV significantly increased the number
638 of Ca^{2+} spikes/enteroid (Fig. 10F) and that the Ca^{2+} spike amplitudes are also
639 substantially greater in RV-infected than in mock-infected jHIE-GCaMP6s enteroids
640 (Fig. 10G). Thus, the RV-induced Ca^{2+} signaling in enteroids closely parallels that
641 observed in MA104 cells and demonstrate that these dynamic Ca^{2+} signals are a
642 biologically relevant aspect of how RV disrupts host Ca^{2+} homeostasis.
643 Since SOCE played a prominent role in the RV-induced dynamic Ca^{2+} signaling
644 in MA104 cells, we investigated whether it was also critical for the Ca^{2+} signaling
645 observed in HIEs. Similar to MA104 cells, jejunum-derived HIEs expressed the core
646 SOCE proteins Orai1, STIM1, and STIM2, as well as the non-store operated Orai3
647 channel (Fig. 11A). The expression levels were not substantially altered by
648 differentiating the jHIEs through removal of growth factors. To test whether SOCE is
649 important for RV-induced Ca^{2+} signaling, we first tested 2-APB treatment of 3D jHIE-

650 GCaMP6s enteroids either mock- or RV-infected with strain Ito. While RV infection
651 increased the number of Ca^{2+} spikes per enteroid consistent with above (Fig. 11B), 2-
652 APB treatment did not attenuate the Ca^{2+} signaling (Fig.11B-C). We speculated that the
653 3D format or the Matrigel used to support 3D HIEs might interfere with 2-APB blocking
654 SOCE, so we repeated these studies using jHIE-GCaMP6s monolayers. First, we
655 confirmed that 2-APB can block thapsigargin-induced SOCE in jHIE-GCaMP6s
656 monolayers, which exhibited a 32% reduction in Ca^{2+} re-entry after store depletion (Fig.
657 11D). Interestingly, 2-APB shows a much less potent block of SOCE in enteroids than in
658 MA104 cells, which exhibited a >80% inhibition of Ca^{2+} re-entry after store depletion
659 (Fig. 9C). We also tested if VACC or NCX may contribute to RV-induced Ca^{2+} signaling
660 in enteroids, but treatment with D600 or KB-R7943 did not reduce Ca^{2+} spikes in RV-
661 infected jHIE-GCaMP6s monolayers (Fig. 11E). Nevertheless, 2-APB treatment of both
662 mock-inoculated (Fig. 11F, black vs. grey traces) and RV-infected jHIE-GCaMP6s
663 monolayers (Fig. 11F, red vs. blue traces) reduced the observed Ca^{2+} signaling, as
664 illustrated in the representative traces (see Supplementary Video 10 online). We
665 quantitated the Ca^{2+} signaling per FOV and confirmed that 2-APB treatment significantly
666 reduced the number of Ca^{2+} spikes for both mock and RV-infected enteroids (Fig. 11G),
667 as well as substantially reducing the amplitude of the Ca^{2+} signals (Fig. 11H). Thus, like
668 the MA104 model, SOCE is critical for supporting the dynamic Ca^{2+} signaling induced in
669 RV-infected jHIEs.

Discussion

A hallmark of RV infection, and several other viruses, is an elevation in cytosolic Ca^{2+} and decrease in ER Ca^{2+} stores, which facilitates virus replication and contributes to pathogenesis through a variety of downstream pathways [1,46]. The importance of RV-induced dysregulation of Ca^{2+} levels for many of these downstream pathways has been determined, but thus far characteristics of the Ca^{2+} signaling itself have not been extensively investigated[1,5]. Thus, the primary goal of this study was to determine the nature of the RV-induced elevation in cytosolic Ca^{2+} and characterize how the dysregulation of Ca^{2+} signaling manifests during the infection. By leveraging GECI-expressing cell lines to perform long-term Ca^{2+} imaging, we found that RV induces a vast increase in Ca^{2+} signaling events that increased in frequency and magnitude over the course of the infection. These results are consistent with previous measurements of cytosolic Ca^{2+} in RV-infected cells that show a monophasic increase over time, which is similar to our imaging data when it is averaged out across the whole FOV (*i.e.*, a cell population). Yet, what is paradigm changing is that at the individual cell level, RV does not merely cause a steady increase in cytosolic Ca^{2+}, but rather activates a cacophony of discrete Ca^{2+} signaling events. Further, by generating GECI-expressing HIEs, this study is the first characterization of RV-mediated Ca^{2+} signaling in normal, human small intestinal enterocytes. We found that the prominence of the Ca^{2+} spikes in RV-infected HIEs is similar to that in MA104 cells, underlining that this is a biologically relevant phenomenon.

The characterization of the RV-induced increase in cytosolic Ca^{2+} as a series of discrete, transient Ca^{2+} signals is an important new insight into the cellular

693 pathophysiology of RV infection. Transient increases in cytosolic Ca^{2+} serve as pro-
694 survival signals by activating phosphoinositide 3-kinase (PI3K) and by calcineurin-
695 dependent NFAT activation. Further, Ca^{2+} oscillations stimulate mitochondrial Ca^{2+}
696 uptake that enhances ATP synthesis, and this increase in mitochondrial metabolism
697 contributes to cell survival pathways. In contrast, strong sustained elevation of cytosolic
698 Ca^{2+} drives pro-apoptotic signaling through mitochondrial Ca^{2+} overload[20]. Thus, even
699 though the mean cytosolic Ca^{2+} level is progressively increasing in the RV-infected cell,
700 early activation of the intrinsic apoptotic cascade may be prevented because it occurs
701 as hundreds of transient Ca^{2+} signals over hours. This premise is consistent with
702 studies showing that early activation of PI3K during RV infection delays apoptosis[47].
703 Concomitantly, the elevated Ca^{2+} signaling activates cellular pathways, such as
704 autophagy, that promote RV replication and assembly of progeny virus[29]. Whether the
705 initial Ca^{2+} dynamics enhance mitochondria bioenergetics or ATP synthesis early during
706 RV infection has not been studied, but a loss of mitochondria membrane potential and
707 decrease in ATP output occur at late stages of infection[47,48]. Ultimately the massive
708 increase in Ca^{2+} signaling damages the cell and triggers cell death, and cell lysis was
709 observed in our time-lapse imaging, but this data cannot differentiate whether this was
710 through apoptosis, necrosis, and/or pyroptosis[18,47,49]. Thus, RV exploitation of discrete
711 Ca^{2+} signals, rather than a sustained increase in cytosolic Ca^{2+}, may function in concert
712 with other RV anti-apoptotic proteins, such as NSP1, to forestall the onset of cell death
713 and enable sustained viral replication.

714 Due to GECI photostability, we were, for the first time, able to perform Ca^{2+}
715 imaging of individual cells throughout the RV infection. The increased Ca^{2+} spikes are

716 the predominant feature of this imaging, and the SA11-mRuby reporter virus
717 demonstrates that the onset of the increased Ca^{2+} signaling correlates with RV protein
718 synthesis as well as input virus dose. Yet, despite individual cells exhibiting very distinct
719 Ca^{2+} signaling traces, a general pattern emerges: [i] early in infection Ca^{2+} signaling
720 remains at basal levels; [ii] onset of increased Ca^{2+} signaling is characterized by low-
721 amplitude Ca^{2+} spikes relatively; and then [iii] very high-amplitude Ca^{2+} spikes become
722 predominant, which results in elevated cytosolic Ca^{2+} levels. The progression of the RV-
723 induced Ca^{2+} signals have important implications for characterizing how Ca^{2+}-regulated
724 cellular processes are influenced by RV infection. For example, RV induces autophagy
725 through increased cytosolic Ca^{2+}, thereby activating calcium/calmodulin-dependent
726 kinase kinase-β (CaMKKβ)[29]. This raises several questions: *When* after onset of the
727 aberrant Ca^{2+} signaling is CaMKKβ activated? *How many* Ca^{2+} signals are needed to
728 induce autophagy? Similar questions can be asked about the role of these Ca^{2+} signals
729 in RV-induced apoptosis, cytoskeletal rearrangement, and serotonin and chloride
730 secretion[26,47,50,51]. Tracking these dynamic relationships poses a challenge that may be
731 addressed by further engineering GECI-expressing cell lines/HIEs to express other
732 biosensors such that both processes can be measured throughout the infection.
733 Many studies show that RV infection (or NSP4 expression) reduces the ER Ca^{2+}
734 stores based on a blunted cytosolic Ca^{2+} release in response to agonists (*e.g.*, ATP) or
735 thapsigargin treatment to prevent SERCA-mediated refilling[22,52]. However, other results
736 show increased in radioactive $^{45}Ca^{2+}$ loading into the ER in RV-infected cells, which is
737 hypothesized to be due to an increase in Ca^{2+} binding proteins (*e.g.*, VP7 or ER
738 chaperone proteins)[7,11]. Thus, controversy remains about whether RV causes a

739 decrease in the ER Ca^{2+} store. To address this question, we developed MA104-
740 RGECO1.2/GCEPIAer cells to directly measure cytosolic and ER Ca^{2+} together during
741 the RV infection. RV induces a dynamic decrease in ER Ca^{2+} levels that occurs in
742 conjunction with the increase in cytosolic Ca^{2+} signaling. In most instances, the cytosolic
743 Ca^{2+} spike correlated with a decrease in ER Ca^{2+}, indicating release of ER Ca^{2+}
744 substantially contributes to the increased cytosolic Ca^{2+} signaling. Further, despite the
745 30% reduction in steady-state ER Ca^{2+}, the dynamic nature of the ER Ca^{2+} signaling
746 suggests that SERCA pumps continually work to refill the ER. The observed depletion
747 of ER Ca^{2+} levels is consistent with the blunted cytosolic response to Ca^{2+} agonists like
748 ATP, the NSP4 function as a Ca^{2+}-conducting viroporin in the ER, and the activation of
749 the ER Ca^{2+} sensor STIM1[7,9,10]. In contrast, it is more difficult to reconcile the previously
750 observed increase in $^{45}Ca^{2+}$ loading into the ER with the 30% reduction in steady-state
751 ER Ca^{2+} levels detected by GCEPIAer imaging in this study. It has been hypothesized
752 that increased $^{45}Ca^{2+}$ loading may be due to increased ER Ca^{2+} buffering capacity,
753 caused by the high levels of RV VP7 and/or chaperones BiP and endoplasmin[11].
754 However, our data suggest this is unlikely to be the case because this would sequester
755 Ca^{2+} and render GCEPIAer unresponsive to changes in ER Ca^{2+}[24], yet this is not the
756 case because GCEPIAer remains dynamic throughout the infection. Alternatively, the
757 increase $^{45}Ca^{2+}$ may reflect loading into the ER-derived autophagy-like microdomains
758 that surround viroplasms, which we observed form after the initial depletion in ER Ca^{2+}
759 and during a partial recovery of ER stores[29,53]. These ER microdomains are the site
760 VP7 assembly onto nascent RV particles, which requires high Ca^{2+}, so Ca^{2+}
761 sequestration in these microdomains may occur independently of the rest of the ER.

762 Future studies using GCEPIAer and viroplasm-targeted GECIs are needed to determine
763 whether the ER and viroplasm-associated membranes are functionally distinct
764 compartments.

765 The pleiotropic functions of NSP4 are responsible for the RV-mediated
766 dysregulation of host Ca^{2+} homeostasis through the ion channel function of iNSP4 and
767 Ca^{2+} agonist function of the secreted eNSP4 enterotoxin [5,9,10]. Our data show that NSP4
768 governs the dynamic Ca^{2+} signaling induced by RV infection since NSP4 knockdown
769 significantly abrogated the number and amplitude of the Ca^{2+} spikes. Unfortunately, it is
770 not possible to determine the relative roles of iNSP4 versus eNSP4 in the induction of
771 the Ca^{2+} spikes from these data because the shRNA decreased total NSP4 synthesis,
772 and therefore both pathways would be attenuated. The importance of NSP4 for the Ca^{2+}
773 signaling is also demonstrated by the extremely different Ca^{2+} signaling profiles of
774 OSUa- and OSUv-infected cells. These differences correlate with the attenuated
775 elevation of cytosolic Ca^{2+} caused by recombinant OSUa NSP4 both when expressed in
776 Sf9 cells (*i.e.*, iNSP4) and exogenous treatment of cells (*i.e.*, eNSP4)[40]. The attenuated
777 NSP4 phenotype is the result of mutations in the NSP4 enterotoxin domain, indicating
778 that this domain is critical for induction of the Ca^{2+} spikes by OSU[25,40]. However, it is
779 important to note that these two viruses are not isogenic so the genetic backgrounds of
780 the OSUa and OSUv NSP4 are different, requiring further Ca^{2+} imaging studies using
781 recombinant RV bearing these attenuating NSP4 mutations to fully dissect the relative
782 importance iNSP4- and eNSP4-mediated Ca^{2+} signaling.

783 NSP4 is the trigger of the dynamic Ca^{2+} signaling, yet these signals are
784 maintained through host Ca^{2+} channels and signaling pathways both in the ER and PM.

785 Removal of extracellular Ca^{2+} significantly attenuated the Ca^{2+} spikes, demonstrating
786 that Ca^{2+} influx is crucial for these signals. Three classes of Ca^{2+} channels (SOCE,
787 NCX, and VACC) have been implicated RV-induced Ca^{2+} influx[10-12,23]. Our results using
788 different pharmacological blockers indicate SOCE is the primary Ca^{2+} influx pathway
789 that supports the RV-induced dynamic Ca^{2+} spikes, both in MA104 cells and in HIEs.
790 Blocking SOCE significantly reduced the number and amplitude of the RV-induced Ca^{2+}
791 spikes. However, the Orai1 SOCE channel is a very low conductance channel so Ca^{2+}
792 entry through PM Orai1 is unlikely to generate the high amplitude Ca^{2+} spikes observed
793 during RV infection. The nature of the Ca^{2+} spikes, and the fact that most of them
794 coincide with ER Ca^{2+} troughs, indicates that the signals detected are ER Ca^{2+}-release
795 events. ER Ca^{2+} release could occur either through iNSP4 or activation of the IP^3-
796 Receptor Ca^{2+} channel, and SOCE serves to maintain these signals by sustaining ER
797 Ca^{2+} refilling. Since elevated Ca^{2+} levels are critical for RV replication, the attenuated
798 Ca^{2+} signaling caused by the SOCE blockers significantly reduced RV yield[29].
799 Interestingly, blocking SOCE in HIEs significantly reduced the Ca^{2+} spikes, but the
800 effect was less pronounced than in MA104 cells, suggesting other pathway(s) may exist
801 that support RV-induced Ca^{2+} spikes in HIEs.
802 In summary, RV dysregulates host Ca^{2+} homeostasis by a massive and
803 progressive increase in discrete Ca^{2+} signaling events, mainly from ER Ca^{2+} release.
804 Many viruses elevate cytosolic Ca^{2+} and alter ER Ca^{2+}, leading us to question whether
805 dynamic Ca^{2+} spikes, as seen in RV infection, is a common manifestation for virus-
806 induced Ca^{2+} signaling. If so, the host channels that support these Ca^{2+} signals, such as

807 Orai1, may represent novel targets for broadly acting host-directed antiviral

808 therapeutics.

Acknowledgments. We would like to thank Dr. Lennart Svensson and Dr. Marie Hagbom for sharing their stocks of the porcine OSUa and OSUv viruses. This work was supported in part by NIH grants K01DK093657, R03DK110270, R01DK115507 (PI: J. M. Hyser), and R01AI080656 and U19AI116497 (PI: M. K. Estes). Trainee support for A.C.G. was provided by NIH grants F30DK112563 (PI: A.Chang-Graham) and the BCM Medical Scientist Training Program and support for both A.C.G. and A.C.S was provided by the Integrative Molecular and Biomedical Sciences Graduate Program (T32GM008231, PI: D. Nelson). This project was supported in part by PHS grant P30DK056338, which supports the Texas Medical Center Digestive Diseases Center (TMC-DDC) Gastrointestinal Experimental Model Systems (GEMS) Core and the Cellular and Molecular Morphology Core. Funding support for the BCM Integrated Microscopy Core includes the NIH (DK56338, CA125123), CPRIT (RP150578, RP170719), the Dan L. Duncan Comprehensive Cancer Center, and the John S. Dunn Gulf Coast Consortium for Chemical Genomics. We would like to thank Xi-Lei (Shelly) Zeng and Xiaomin Yu for their help with enteroid cultures and media, and Drs. Michael Mancini and Fabio Stossi for deconvolution microscopy assistance. FACS sorting of cell lines utilized the BCM Cytometry and Cell Sorting Core with funding from the CPRIT Core Facility Support Award (CPRIT-RP180672), the NIH (CA125123 and RR024574), and the expert assistance of Joel M. Sederstrom.

Author Contributions. JH, ACG, JP, AS, JC and MKE designed the experiments and discussed the data. JH, ACG, JP, NR, and AS conducted the calcium imaging experiments and analyzed the data with JH and ACG. JC and MKE provided key reagents including the shRNA knockdown cells. JP conducted the western blot and plaque assays and analyzed data with JH. AS and ACG conducted and analyzed qPCR experiments. JH and ACG wrote the manuscript, and all authors contributed to revisions of the paper.

Table 1: Primers used in this work

Gene	Species	Forward (5') Sequence	Reverse (3') Sequence
18S	Universal	CGCCTTCCTCTTCGAGTATGA	AGATAACGCCCACCTTCTTATTACG
STIM1	Universal	TCATTGGAGCATGAGTGGAT	AGGTGTGGGTGGGAGTAGAG
STIM2	Human	CAGTCTTTGGGACTCTGCACGT	GCCAGCGAAAAAGTCGTTCTCG
STIM2	African green monkey	CAAGTTGCCCTGCGCTTTAT	TGCAGCTCTCGAGTTTTCCT
Orai1	Human	CCCTTCGGCCTGATCTTTAT	CAGTGAGCGGTAGAAGTGGA
Orai1	African green monkey	TTGCTCGCTTACAGGACCAG	AAGGGCGTAAGGCCAAAGAA
Orai2	Human	CCTGTCGTGGCGGAAGCTCTA	ACTGGTACTGCGTCTCCAGCTG
Orai2	African green monkey	CTGGGCCACAGGCCAC	AGGAGTAGAGGGGTCGACAG
Orai3	Human	TTCCAGCCGCACGTCTGCCTT	CACGGTGGTGCAGGCACTGAA
Orai3	African green monkey	CCCAGGCATTGGTCTAGCTT	GTTTGGTGCATAGCGTGGTG

Figures

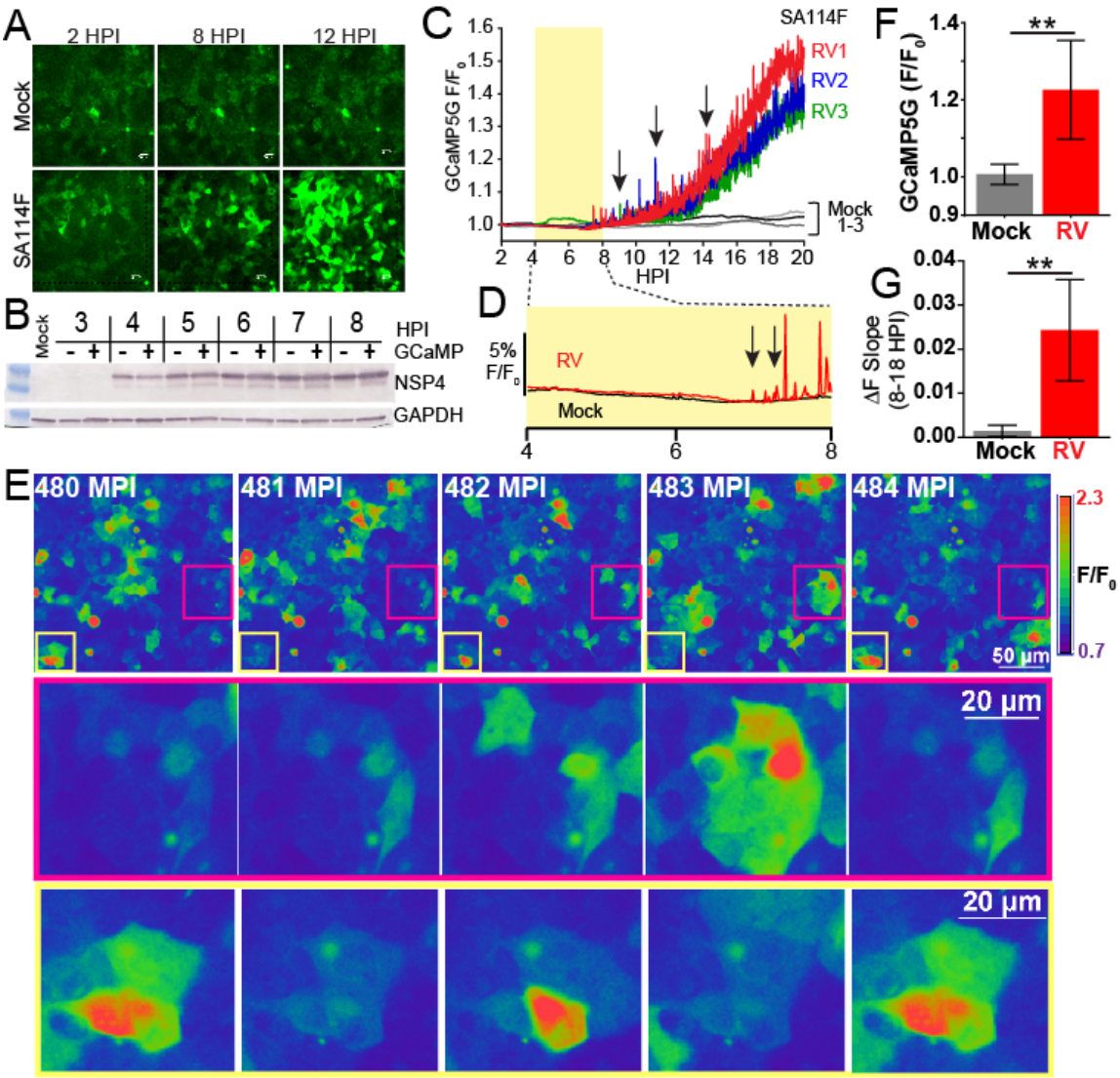

Figure 1. RV-induced increase in cytosolic Ca^{2+} manifests as increased Ca^{2+} signaling dynamics. (A) Epifluorescence images of mock (upper) or SA114F-infected (MOI 10) MA104-GCaMP5G cells at 2, 8, and 12 hours post-infection (HPI). **(B)** Western blot of RV NSP4 expression in MA104 cells without (-) or with (+) GCaMP5G from 3-8 HPI. Western blot for GAPDH serves as a loading control. **(C)** GCaMP5G fluorescence (F/F_0) for three fields-of-view (~455 μm^2) each of mock (black and grey lines) or RV-infected (red, blue, and green) MA104-GCaMP5G cells from 2-20 HPI. Increased frequency of transient Ca^{2+} fluxes (arrows) highlight the increased Ca^{2+} signaling dynamics. **(D)** Expanded graph of relative GCaMP5G (F/F_0) of representative Mock (black) and RV-infected (red) cells. Arrows indicate the increased low/moderate amplitude Ca^{2+} signals present during the initial increase in steady-state cytosolic Ca^{2+}. **(E)** Examples of the dynamic Ca^{2+} signaling. GCaMP5G fluorescence pseudocolored by intensity from 480-484 minutes post-infection (MPI). Regions in the magenta and yellow boxes are magnified below. **(F)** Average GCaMP5G fluorescence from 18-19 HPI and **(G)** slope of GCaMP5G ΔF from 8-18 HPI. Data shown as mean ± SD from 12 fields-of-view (triplicate of four independent experiments). **p<0.01

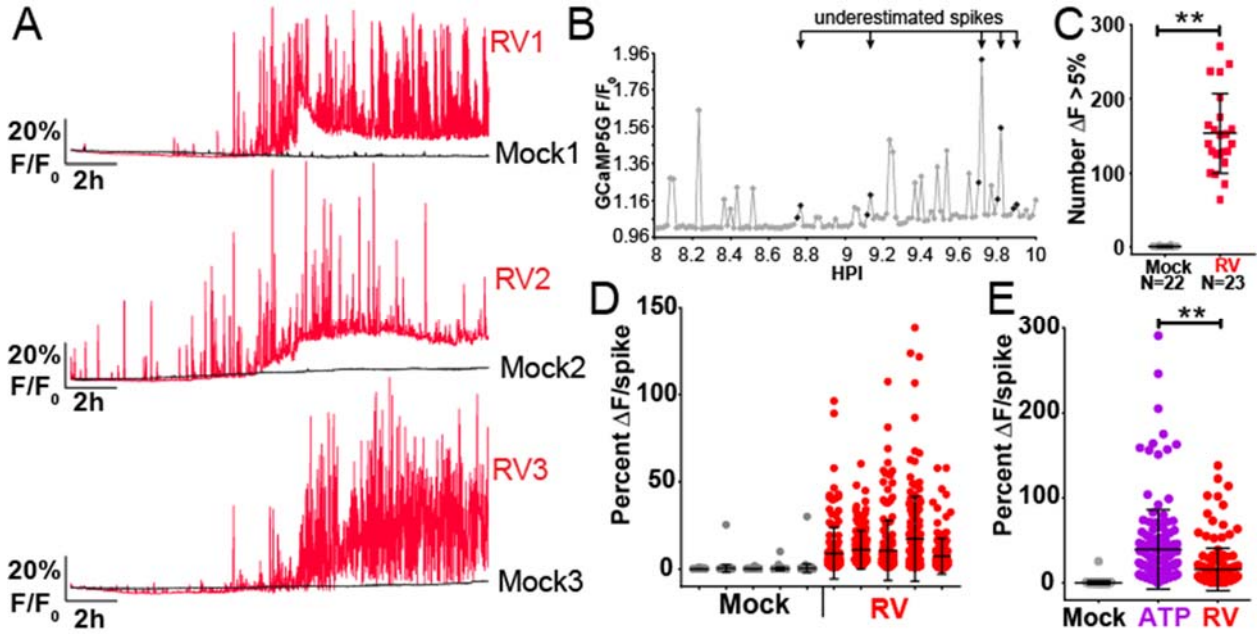

Figure 2. RV increases the number and amplitude of Ca^{2+} spikes at the single-cell level. **(A)** GCaMP5G (F/F_0) fluorescence traces from three representative single mock (black) or RV-infected (red) MA104-GCaMP5G cells. **(B)** GCaMP5G fluorescence (F/F_0) of a single RV-infected MA104-GCaMP5G cell from 8-10 HPI. Symbols in magenta denote Ca^{2+} spikes captured in two data points and potentially underestimated by counting spikes as ΔF >5%. **(C)** MA104-GCaMP5G cells mock or RV infected (MOI 10), GCaMP5G fluorescence was imaged from 2-20 HPI and the number of Ca^{2+} spikes (ΔF >5%) individual cells was determined. **(D)** Ca^{2+} spike amplitude of the top 150 Ca^{2+} spikes from five representative mock and RV-infected cells. **(E)** GCaMP5G Ca^{2+}response to 50 μM ATP in comparison to mock or RV infection. Data shown as mean ± SD. **p<0.01

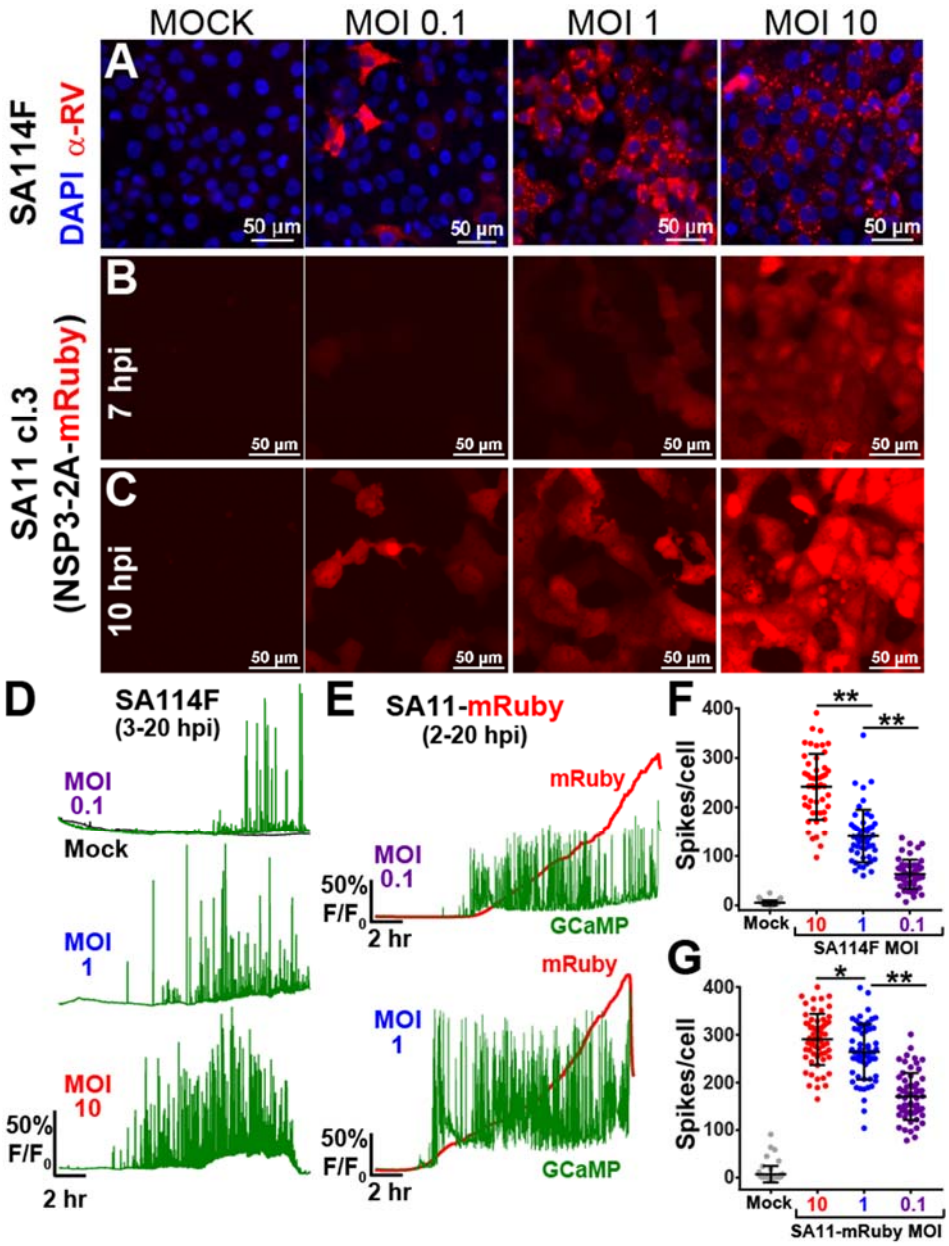

Figure 3. RV-induced dynamic Ca^{2+} signaling is related to virus dose. (A) Immunofluorescence images of mock or SA114F-infected MA104-GCaMP5G cells that were inoculated with increasing MOI (0.1, 1, or 10). RV antigen (red) is detected at ~8 hpi with anti-RV polyclonal antisera and nuclei are stained with DAPI (blue). **(B-C)** Epifluorescence images of MA104-GCaMP5G cells mock or infected with recombinant SA11-mRuby reporter virus with increasing MOIs (0.1, 1, 10). Images were captured at 7 HPI **(B)** or 10 HPI **(C)**. **(D)** Representative single-cell traces of relative GCaMP5G fluorescence (F/F_0) from cells mock (black) or RV infected by SA114F with MOIs of 0.1 (purple), 1 (blue), 10 (red). **(E)** Representative single-cell traces of relative fluorescence (F/F_0) of GCaMP5G (green) and mRuby (red) from cells infected by SA11-mRuby MOI 0.1 (purple) or 1 (blue). **(F-G)** Number of Ca^{2+} spikes (F/F_0 > 5%) from mock or RV-infected cells that were infected with SA114F **(F)** or SA11-mRuby **(G)**. Data shown as mean ± SD of 60 cells/condition. **p<0.01

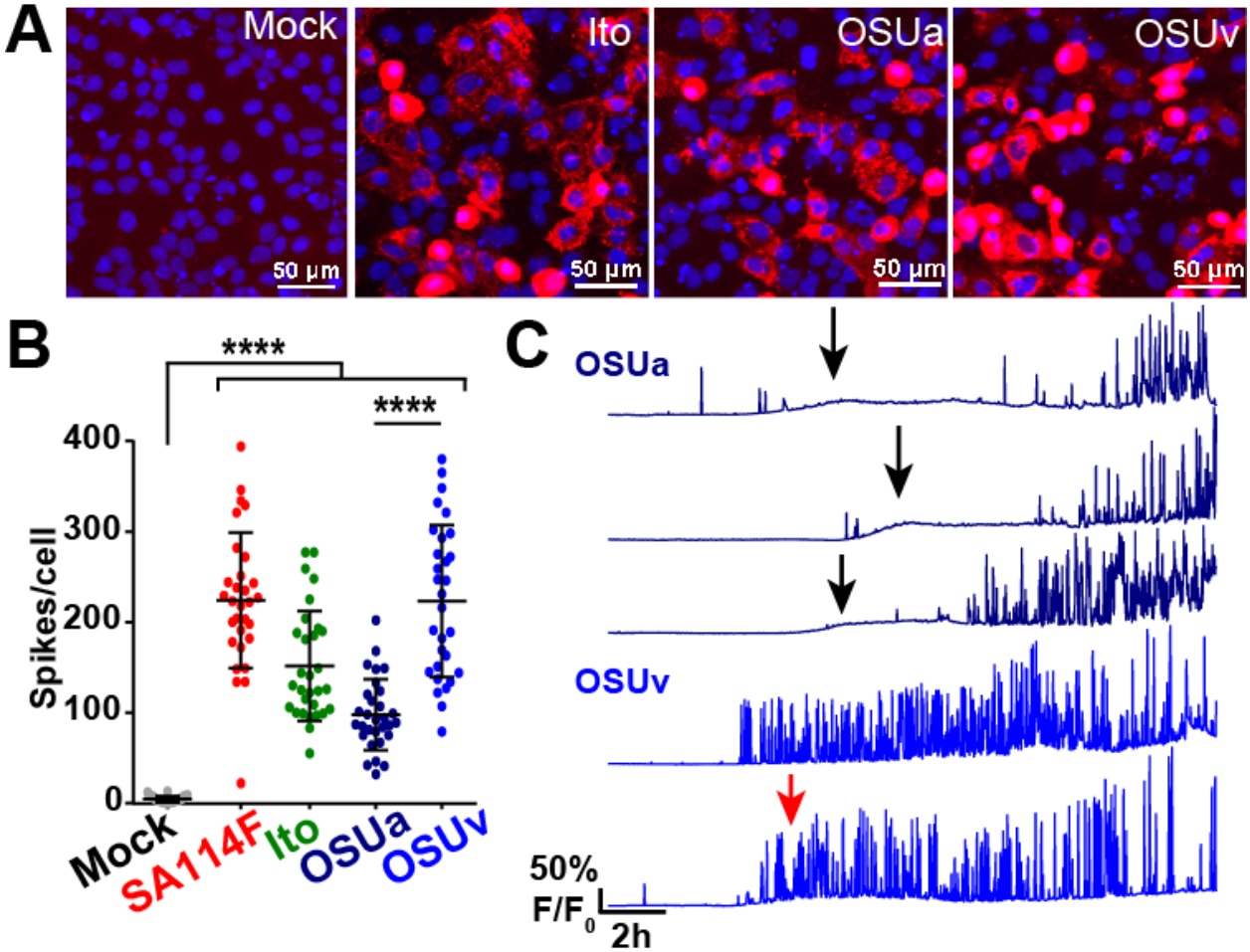

Figure 4. Dynamic Ca^{2+} signaling is induced by several other RV strains. (A) Immunofluorescence images of MA104-GCaMP5G cells mock or infected by human RV strain Ito, porcine OSUa, or porcine OSUv at MOI 1. RV antigen (red) is detected at ~8 hpi with anti-RV polyclonal antisera and nuclei are stained with DAPI (blue). **(B)** Number of Ca^{2+} spikes (F/F_0 > 5%) from mock or RV-infected cells inoculated with MOI1 of the strains listed. Data shown as mean ± SD of 30 cells/condition. ****$p<0.0001$. **(C)** Representative single-cell traces of relative GCaMP5G fluorescence (F/F_0) from cells infected by OSUa (purple) or OSUv (blue). A slight increase in the steady-state Ca^{2+} level is exhibited by most OSUa-infected (black arrows) and some OSUv-infected (red arrow) cells.

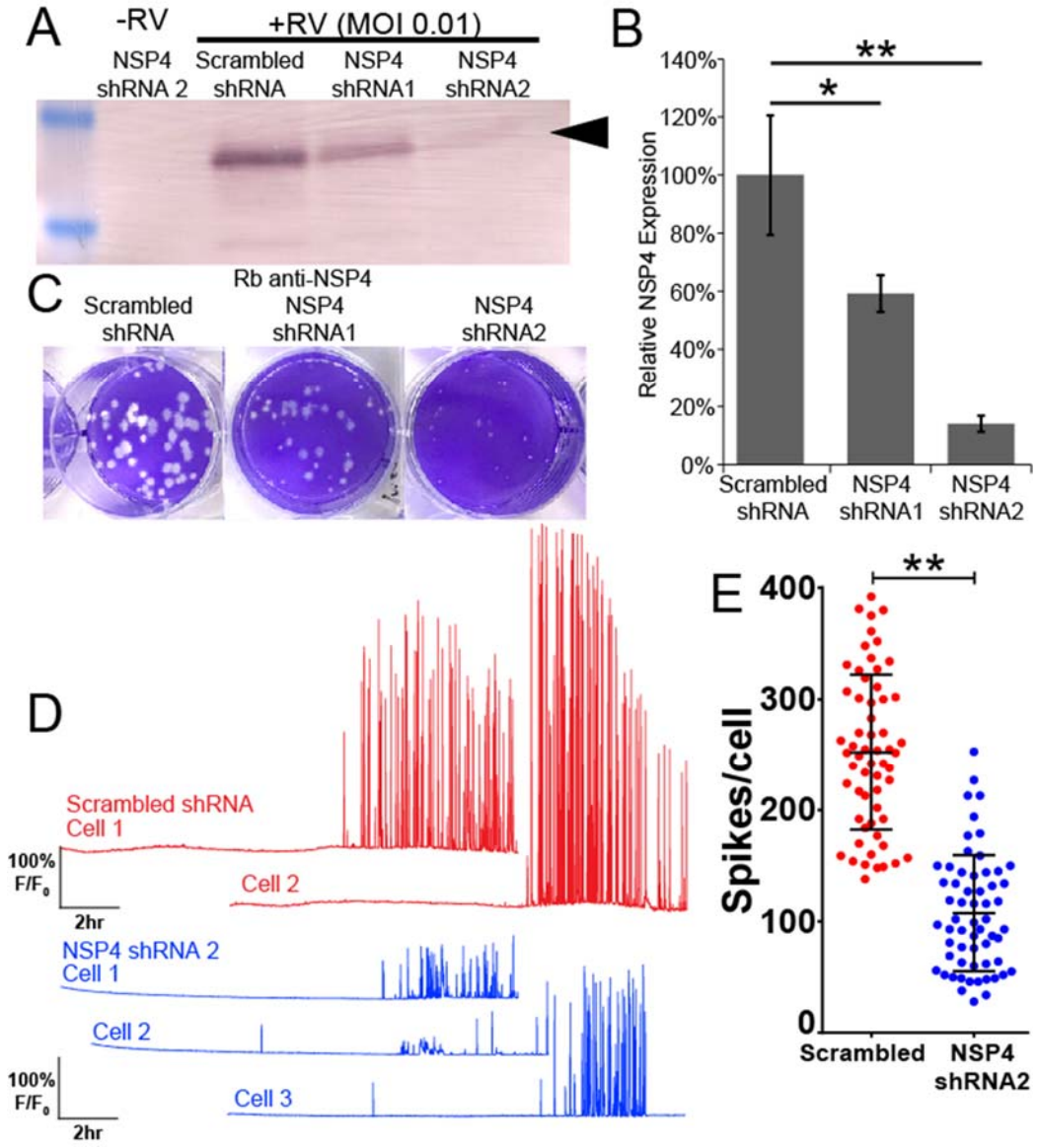

Figure 5. Knockdown of NSP4 reduces the dynamic Ca^{2+} signaling. (A) Western blot for NSP4 expression in mock infected or RV-infected MA104-GCaMP6s/shRNA cell lines. Cells expressing either scrambled, NSP4 shRNA1, or NSP4 shRNA2 are as indicated. Arrow denotes full-length, glycosylated NSP4. **(B)** Densitometry analysis of western blots for NSP4 levels normalized to that of GAPDH levels, expressed as relative to NSP4 expressed in MA104-GCaMP6s/scrambled shRNA cells. Data shown are mean ± SD of 3 infections/condition and representative of 3 independent experiments. **(C)** Plaque assay of MA104-GCaMP6s/shRNA cell lines inoculated with SA114F (10^{-6} dilution). **(D)** Representative single-cell traces of relative GCaMP6s fluorescence (F/F_0) from SA114F infection of cells expressing scrambled shRNA (red) or NSP4 shRNA2 (blue). **(E)** Number of Ca^{2+} spikes (F/F_0 > 5%) from mock or RV-infected cells inoculated with MOI0.1 SA114F. Data shown as mean ± SD of 60 cells/condition. **p<0.01.

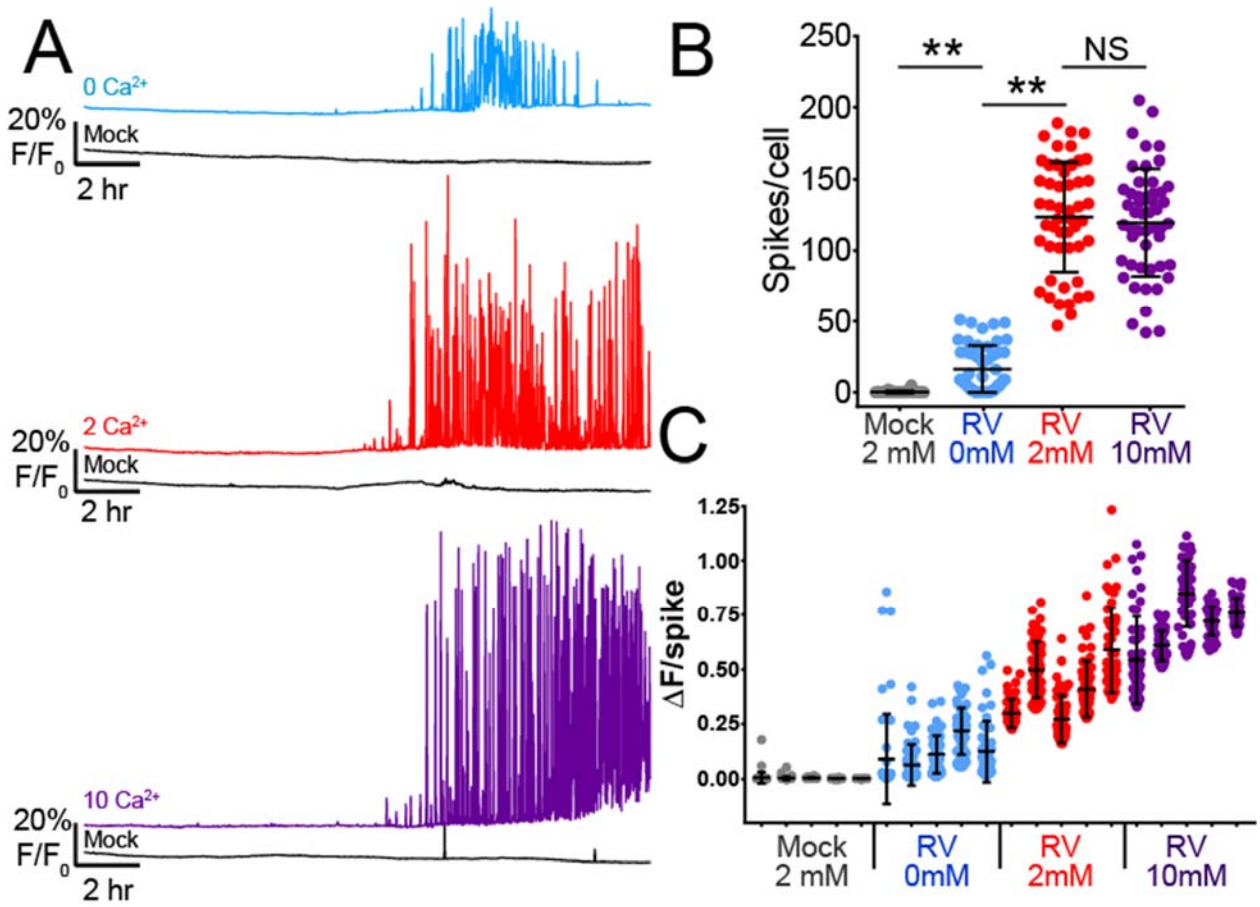

Figure 6. Ca^{2+} signaling requires extracellular Ca^{2+}. (A) Representative single-cell traces of relative GCaMP5G fluorescence (F/F_0) from mock (black lines) or SA114F infected cells in Ca^{2+}-free media ($0Ca^{2+}$, light blue), normal media ($2Ca^{2+}$, red), and high Ca^{2+} media ($10Ca^{2+}$, purple). **(B)** Number of Ca^{2+} spikes (F/F_0 > 5%) from mock or RV-infected cells inoculated with MOI 1 SA114F and maintained in the indicated media. Data shown as mean ± SD of 50 cells/condition. **p<0.01. **(C)** Ca^{2+} spike amplitude of the top 50 Ca^{2+} spikes from five representative mock and RV-infected cells in each media condition.

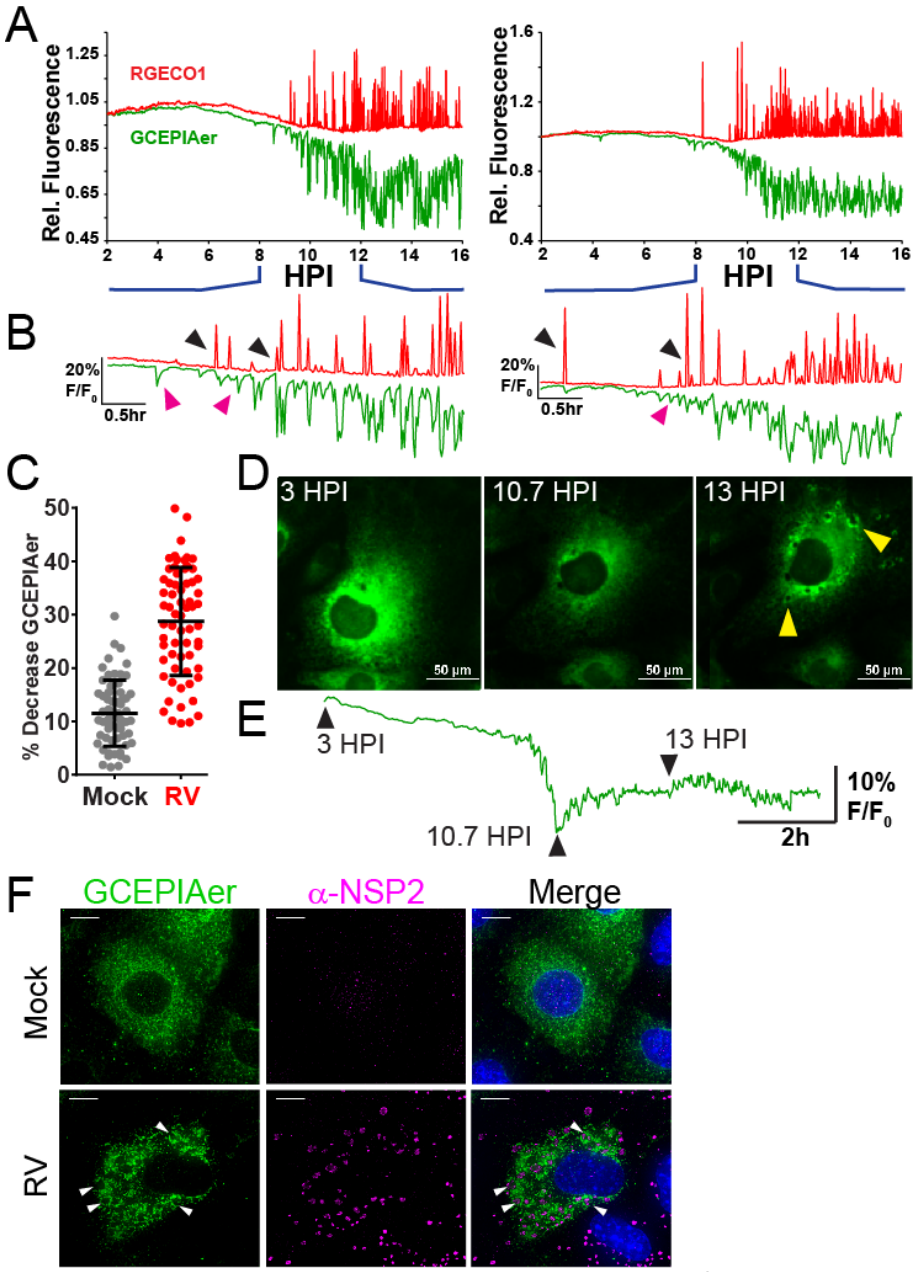

Figure 7. RV induces dynamic decreases in ER Ca^{2+} that coincide with cytoplasmic Ca^{2+} signals. (A) Two representative single-cell traces of relative RGECO1.2 (red) and GCEPIAer (green) fluorescence (F/F_0, both RGECO1.2 and GCEPIAer are shown on the same scale) from MA104-RGECO/GCEPIAer cells infected with SA114F at MOI 1. **(B)** Traces from (A) expanded to show details from 8-12 HPI. Black arrowheads indicate ER Ca^{2+} troughs that correspond to cytoplasmic Ca^{2+} spikes. Magenta arrowheads indicate ER Ca^{2+} troughs that lack a corresponding cytoplasmic Ca^{2+} spike. **(C)** Percent decrease in ER Ca^{2+} levels measured by GCEPIAer fluorescence. **(D-E)** Images of a representative RV-infected MA104-GCEPIAer cell (D) taken at 3, 7.75, and 10 HPI and the corresponding trace from that cell with arrowheads corresponding the images above. Formation of viroplasm structures (yellow arrowheads) are observed subsequent to the decrease in ER Ca^{2+} levels. **(F)** Deconvolution microscopy of mock or RV-infected MA104-GCEPIAer cells (MOI 0.25, fixed 24 hpi) stained with α-NSP2 [Dylight 549 (pink)] to detect viroplasms (white arrowheads). (scale bar = 10 µm)

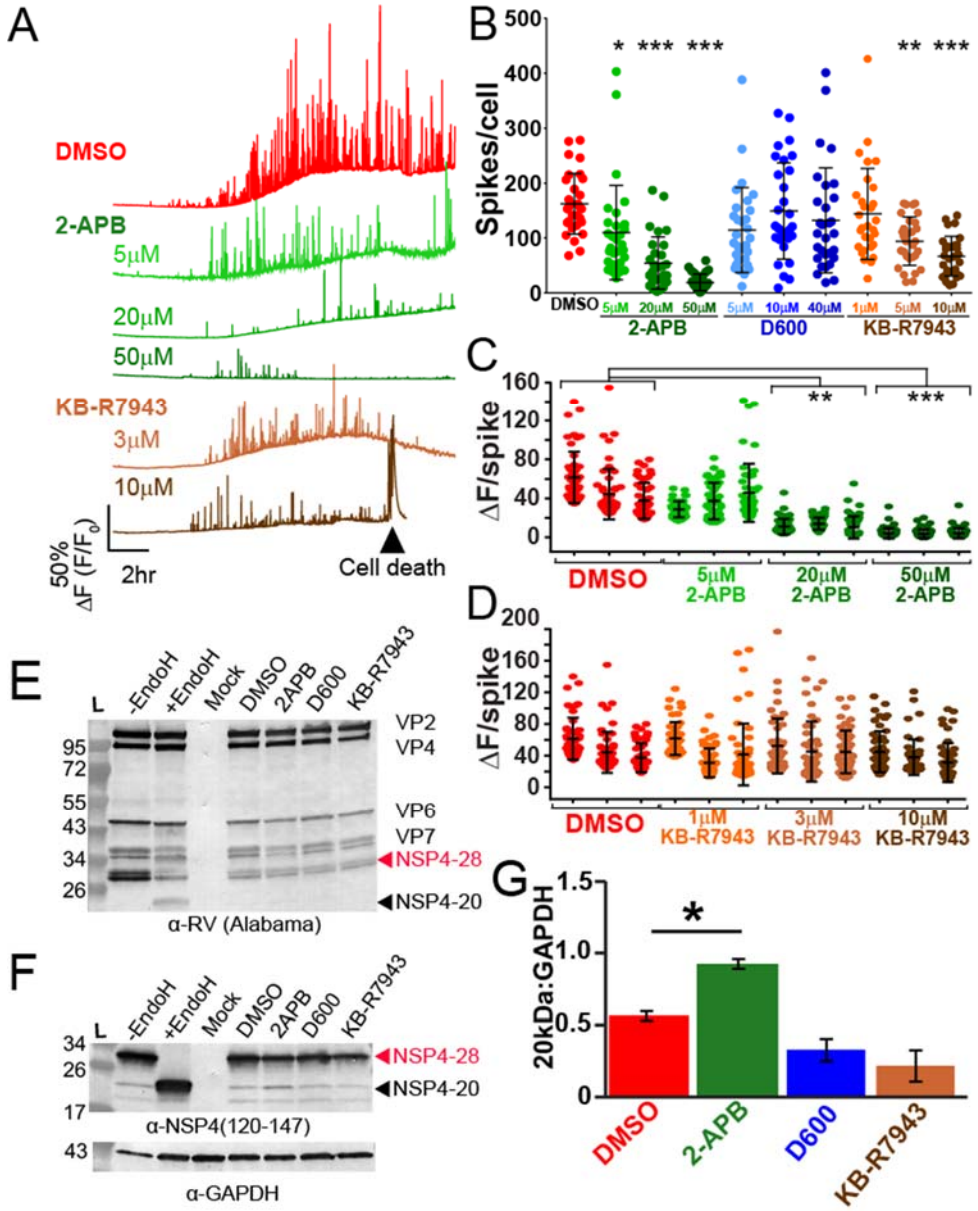

Figure 8. RV-induced Ca^{2+} signaling is blocked by the SOCE blocker 2APB. (A) Representative single-cell traces from MA104-GCaMP5G cells infected with SA114F MOI 1 and treated with DMSO vehicle alone or the indicated doses of 2APB or KB-R7943. Cell death of RV-infected cells treatment with 10 uM KB-R7943 was frequently observed (black arrowhead). **(B)** Number of Ca^{2+} spikes (F/F_0 > 5%) from RV-infected cells inoculated with MOI 1 and treated with the indicated concentration of 2APB, D600 or KB-R7943. **(C-D)** Ca^{2+} spike amplitude of the top 50 Ca^{2+} spikes from three representative RV-infected cells treated DMSO (vehicle) or the indicated concentration of 2APB (C) or KB-R7943 (D). **(E-F)** Western blot analysis of MA104-GCaMP5G cells mock or RV-infected MOI 1 and treated with DMSO (vehicle), 50 μM 2APB, 10 μM D600, or 10 μM KB-R7943. Control RV-infected lysates treated with Endoglycosadase H (+EndoH) or untreated (-EndoH) are also shown. Blots were detected with α-RV (E) or α-NSP4(120-147) (F) and α-GAPDH (F, bottom) was the loading control for both. **(G)** ImageJ analysis of unglycosylated NSP4 (20kDa) normalized to GAPDH from RV-infected cells treated with the different blockers. Data are the mean ± SD of three independent infections per condition. *p<0.05

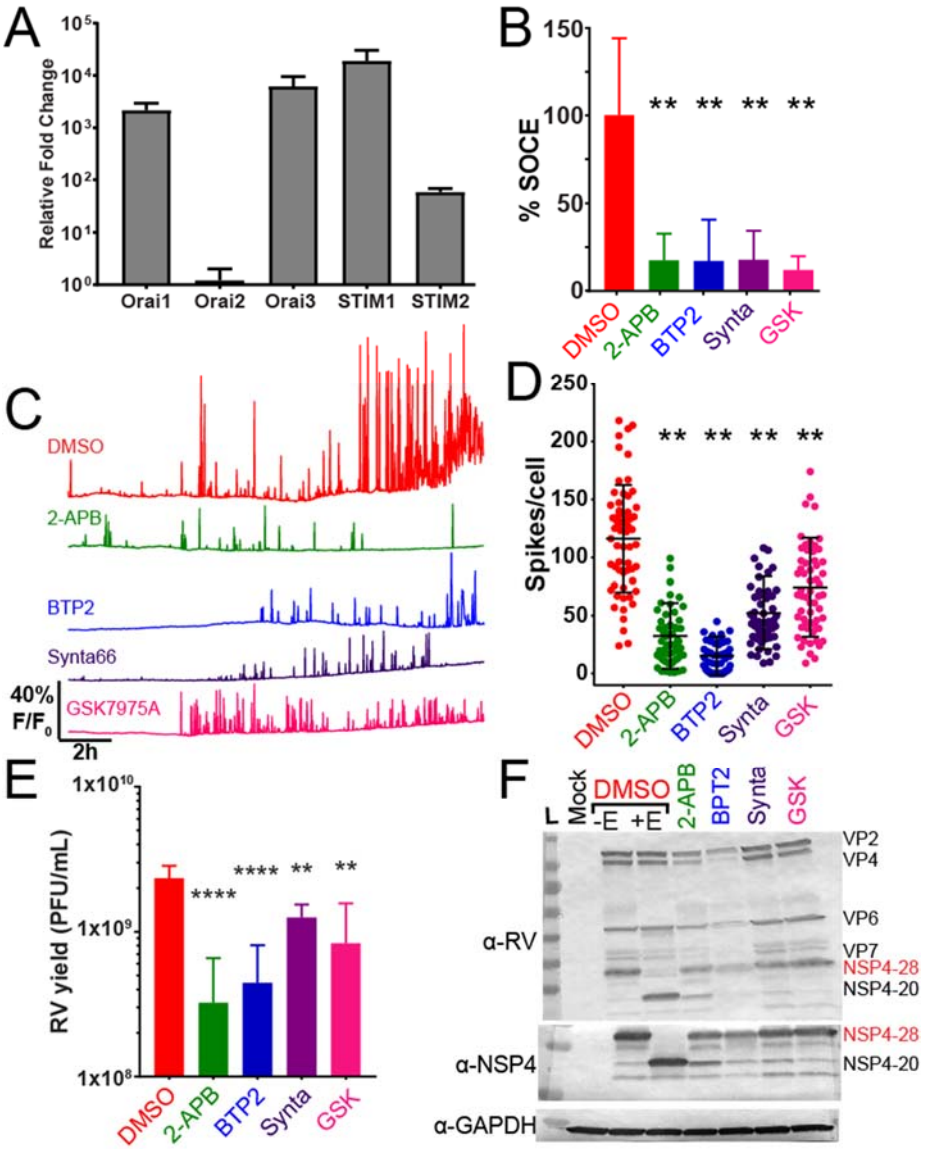

Figure 9. SOCE blockers reduce RV-induced Ca^{2+} signaling. (A) Relative mRNA expression of Orai1-3 and STIM1-2 genes in MA104 cells. Expression is normalized to 16S rRNA and graphed relative to Orai2. **(B)** SOCE was activated by treatment with 0.5 μM thapsigargin in Ca^{2+}-free buffer and the amount of SOCE relative to DMSO-alone (vehicle) for different SOCE blockers determined. Data are the mean ± SD of three independent runs. **p<0.01. **(C)** Representative single-cell traces from MA104-GCaMP5G cells infected with SA114F MOI 1 and treated with DMSO vehicle alone or the indicated doses of 50 μM 2APB, 10 μM BTP2, 10 μM Synta66, or 10 μM GSK7975A. **(D)** Number of Ca^{2+} spikes (F/F_0 > 5%) from RV-infected cells inoculated with MOI 1 and treated with DMSO alone or the SOCE blockers. Data are the mean ± SD 60 cells/condition. **p<0.01 by one-way ANOVA. **(E)** SA114F yield from MA104-GCaMP5G cells treated with DMSO or the SOCE blockers. Data are the mean ± SD of three independent infections. ****p<0.0001; **p<0.01 by one-way ANOVA. **(F)** Western blot analysis of MA104-GCaMP5G cells mock or RV-infected MOI 1 and treated with DMSO or the SOCE blockers. Control RV-infected lysates treated with Endoglycosadase H (+EndoH) or untreated (-EndoH) are also shown. Blots were detected with α-RV, α-NSP4(120-147), and α-GAPDH for the loading control.

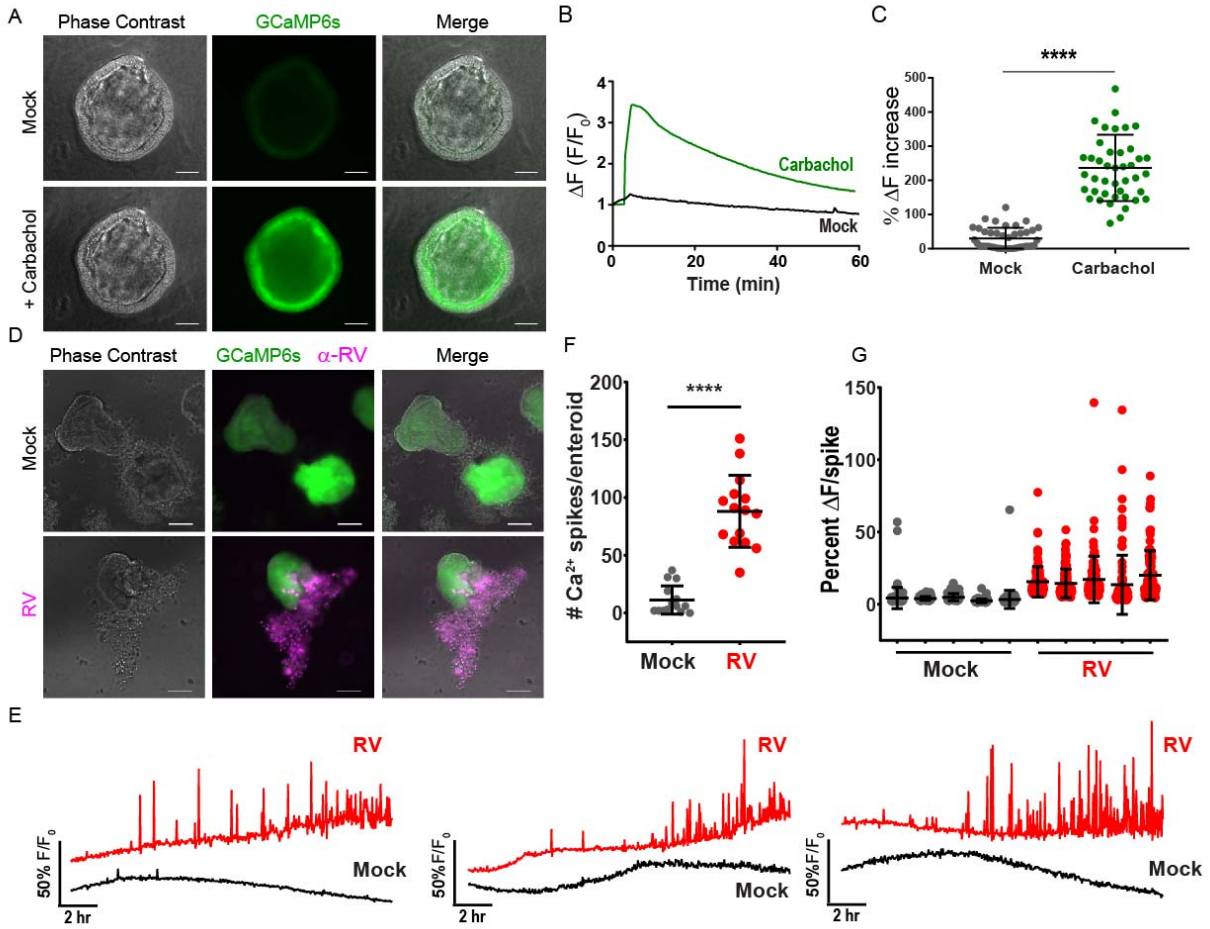

Figure 10. jHIE-GCaMP6s enteroids exhibit dynamic Ca^{2+} signaling during RV infection. **(A)** Representative images of jejunum human intestinal enteroids stably expressing GCaMP6s (jHIE-GCaMP6s) one minute after addition of 200 μM carbachol or media alone (mock). **(B)** Representative trace of jHIE-GCaMP6s treated with 200 μM carbachol or media alone. GCaMP6s fluorescence (F) was normalized to the baseline fluorescence (F_0). **(C)** The maximum % increase in normalized fluorescence after addition of media (mock, N=41) or 200 μM carbachol (N=43), data combined from 3 independent experiments. **(D)** Representative immunofluorescence images of mock and Ito RV-infected jHIE-GCaMP6s (green) fixed at ~24 hpi and stained for RV (pink). **(E)** Representative Ca^{2+} traces of whole jHIE-GCaMP6s enteroids either mock or Ito RV-infected between 6-23 hpi. GCaMP6s fluorescence (F) was normalized to the baseline fluorescence (F_0). **(F)** Number of Ca^{2+} spikes in mock (N=15) or Ito RV-infected (N=15) HIEs and **(G)** the fold change in fluorescence for randomly selected 5 HIEs mock- and RV-infected. Data are representative of one experiment that was performed in triplicate. ****$p<0.0001$, scale bars = 100 μm.

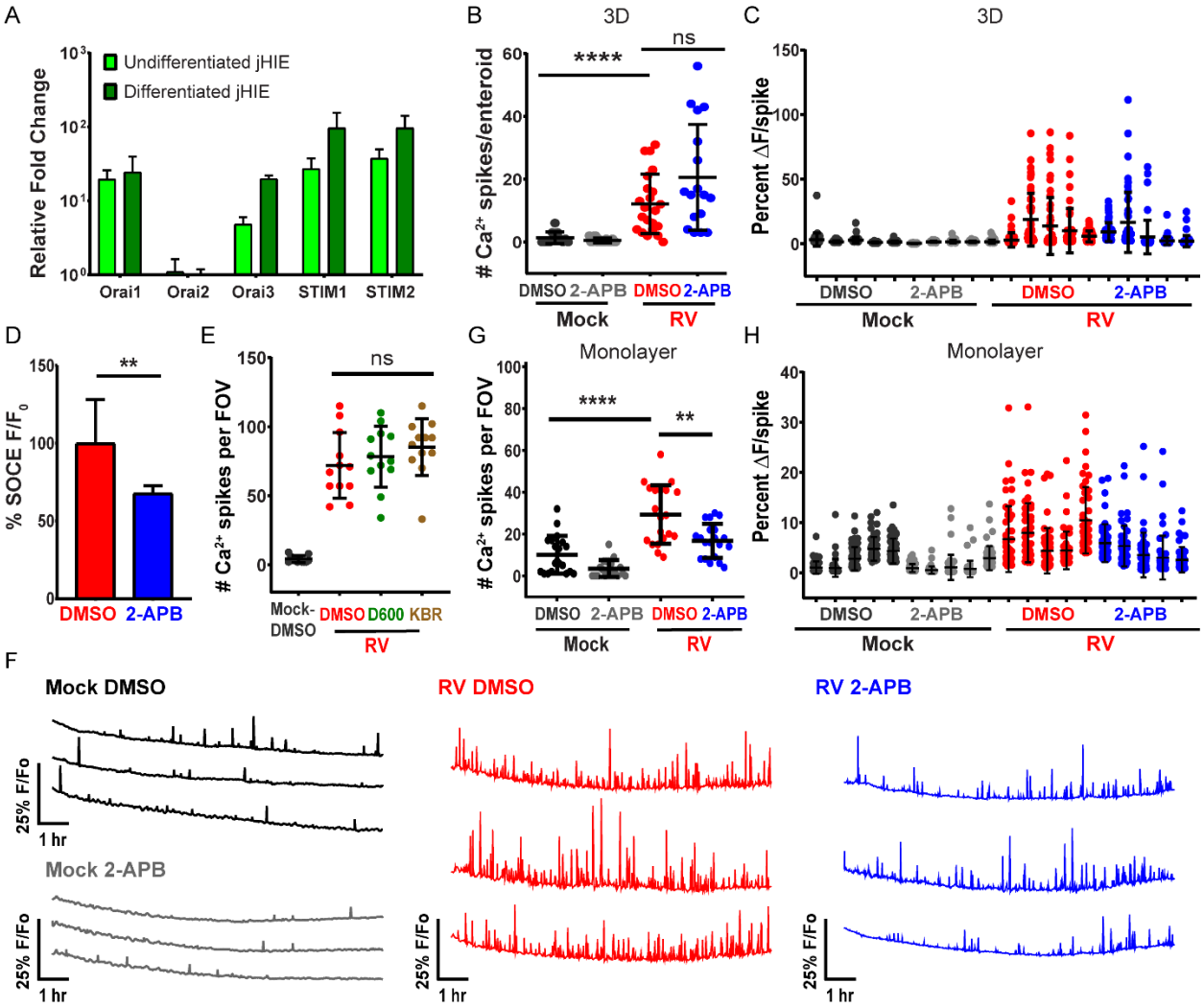

Figure 11. **Blocking SOCE reduces Ca^{2+} signaling during RV infection in jHIE-GCaMP6s monolayers. (A)** qPCR of Orai and stromal interaction molecule (STIM) mRNA transcripts normalized to 18S mRNA transcripts and fold change relative to Orai2 mRNA transcript levels in jejunum human intestinal enteroids (jHIEs), log scale (n = 3 biological replicates). **(B)** Number of Ca^{2+} spikes in 3D jHIE-GCaMP6s mock- or RV-infected and treated with DMSO (N=12, 18) or 50 μM 2APB (N=22, 17) and **(C)** the percent change in fluorescence for the highest 50 Ca^{2+} spikes for 5 HIEs of each condition for 6-18 hpi. GCaMP6s fluorescence (F) was normalized to the baseline fluorescence (F_0). Data are representative of one experiment that was performed in triplicate. **(D)** Number of Ca^{2+} spikes per field-of-view (FOV) in mock- or RV-infected jHIE-GCaMP6s monolayers treated with DMSO, 10 μM D600, or 10 μM KB-R7943 between 8-22 hpi, data combined from 3 experiments. **(E)** Relative fluorescence increase (F/F_0) due to store-operated calcium entry in jHIE-GCaMP6s monolayers after store depletion with 500 nM thapsigargin. Data combined from ≥6 experiments. **(F)** Representative Ca^{2+} traces per FOV of monolayers either mock- or RV-infected and treated with DMSO or 50 μM 2APB between 8-19 hpi. **(G)** Number of Ca^{2+} spikes per FOV and **(H)** the percent change in fluorescence for the highest 50 Ca^{2+} spikes for 5 FOVs of each condition for 8-19 hpi. Data combined from 5 experiments. (**p<0.01, ****p<0.0001)

References

1 Hyser, J. M. & Estes, M. K. Pathophysiological Consequences of Calcium-Conducting Viroporins. *Annu. Rev. Virol* **2**, 473-496, doi:10.1146/annurev-virology-100114-054846 [doi] (2015).

2 Troeger, C. *et al.* Rotavirus Vaccination and the Global Burden of Rotavirus Diarrhea Among Children Younger Than 5 Years. *JAMA Pediatr* **172**, 958-965, doi:10.1001/jamapediatrics.2018.1960 (2018).

3 Thiagarajah, J. R., Donowitz, M. & Verkman, A. S. Secretory diarrhoea: mechanisms and emerging therapies. *Nat. Rev. Gastroenterol. Hepatol* **12**, 446-457, doi:nrgastro.2015.111 [pii];10.1038/nrgastro.2015.111 [doi] (2015).

4 Michelangeli, F., Ruiz, M. C., del Castillo, J. R., Ludert, J. E. & Liprandi, F. Effect of rotavirus infection on intracellular calcium homeostasis in cultured cells. *Virology* **181**, 520-527 (1991).

5 Sastri, N. P., Crawford, S. E. & Estes, M. K. in *Viral Gastroenteritis: Molecular Epidemiology and Pathogenesis* (eds L. Svensson, U. Desselberger, H.B. Greenberg, & M.K. Estes) Ch. 2.4, 145-174 (Elsevier Academic Press, 2016).

6 Tian, P. *et al.* The rotavirus nonstructural glycoprotein NSP4 mobilizes Ca2+ from the endoplasmic reticulum. *J Virol* **69**, 5763-5772 (1995).

7 Diaz, Y. *et al.* Expression of nonstructural rotavirus protein NSP4 mimics Ca2+ homeostasis changes induced by rotavirus infection in cultured cells. *J Virol* **82**, 11331-11343 (2008).

8 Hyser, J. M., Collinson-Pautz, M. R., Utama, B. & Estes, M. K. Rotavirus disrupts calcium homeostasis by NSP4 viroporin activity. *mBio* **1**, e00265-00210 (2010).

9 Pham, T., Perry, J. L., Dosey, T. L., Delcour, A. H. & Hyser, J. M. The Rotavirus NSP4 Viroporin Domain is a Calcium-conducting Ion Channel. *Sci Rep* **7**, 43487, doi:10.1038/srep43487 (2017).

10 Hyser, J. M., Utama, B., Crawford, S. E., Broughman, J. R. & Estes, M. K. Activation of the endoplasmic reticulum calcium sensor STIM1 and store-operated calcium entry by rotavirus requires NSP4 viroporin activity. *J Virol* **87**, 13579-13588 (2013).

11 Diaz, Y. *et al.* Dissecting the Ca(2)(+) entry pathways induced by rotavirus infection and NSP4-EGFP expression in Cos-7 cells. *Virus. Res* **167**, 285-296 (2012).

12 Perez, J. F., Ruiz, M. C., Chemello, M. E. & Michelangeli, F. Characterization of a membrane calcium pathway induced by rotavirus infection in cultured cells. *J Virol* **73**, 2481-2490 (1999).

13 Zhang, M., Zeng, C. Q., Morris, A. P. & Estes, M. K. A functional NSP4 enterotoxin peptide secreted from rotavirus-infected cells. *J Virol* **74**, 11663-11670 (2000).

14 Dong, Y., Zeng, C. Q., Ball, J. M., Estes, M. K. & Morris, A. P. The rotavirus enterotoxin NSP4 mobilizes intracellular calcium in human intestinal cells by stimulating phospholipase C-mediated inositol 1,4,5-trisphosphate production. *Proc. Natl. Acad. Sci. U. S. A* **94**, 3960-3965 (1997).

15 Ball, J. M., Tian, P., Zeng, C. Q., Morris, A. P. & Estes, M. K. Age-dependent diarrhea induced by a rotaviral nonstructural glycoprotein. *Science* **272**, 101-104 (1996).

16 Morris, A. P. *et al.* NSP4 elicits age-dependent diarrhea and Ca(2+)mediated I(-) influx into intestinal crypts of CF mice. *Am. J Physiol* **277**, G431-G444 (1999).

17 Ousingsawat, J. *et al.* Rotavirus toxin NSP4 induces diarrhea by activation of TMEM16A and inhibition of Na+ absorption. *Pflugers. Arch* **461**, 579-589 (2011).

18 Perez, J. F., Chemello, M. E., Liprandi, F., Ruiz, M. C. & Michelangeli, F. Oncosis in MA104 cells is induced by rotavirus infection through an increase in intracellular Ca2+ concentration. *Virology* **252**, 17-27 (1998).

19 Brunet, J. P. *et al.* Rotavirus infection induces an increase in intracellular calcium concentration in human intestinal epithelial cells: role in microvillar actin alteration. *J Virol* **74**, 2323-2332 (2000).
20 Tanwar, J. & Motiani, R. K. Role of SOCE architects STIM and Orai proteins in Cell Death. *Cell Calcium* **69**, 19-27, doi:S0143-4160(17)30059-3 [pii];10.1016/j.ceca.2017.06.002 [doi] (2018).
21 Soboloff, J., Rothberg, B. S., Madesh, M. & Gill, D. L. STIM proteins: dynamic calcium signal transducers. *Nat Rev Mol Cell Biol* **13**, 549-565 (2012).
22 Zambrano, J. L. *et al.* Silencing of rotavirus NSP4 or VP7 expression reduces alterations in Ca2+ homeostasis induced by infection of cultured cells. *J Virol* **82**, 5815-5824 (2008).
23 Perry, J. L., Ramachandran, N. K., Utama, B. & Hyser, J. M. Use of genetically-encoded calcium indicators for live cell calcium imaging and localization in virus-infected cells. *Methods* **90**, 28-38, doi:S1046-2023(15)30075-X [pii];10.1016/j.ymeth.2015.09.004 [doi] (2015).
24 Suzuki, J. *et al.* Imaging intraorganellar Ca2+ at subcellular resolution using CEPIA. *Nat. Commun* **5**, 4153, doi:ncomms5153 [pii];10.1038/ncomms5153 [doi] (2014).
25 Bialowas, S. *et al.* Rotavirus and Serotonin Cross-Talk in Diarrhoea. *PLoS One* **11**, e0159660, doi:10.1371/journal.pone.0159660 [doi];PONE-D-16-05251 [pii] (2016).
26 Saxena, K. *et al.* Human Intestinal Enteroids: a New Model To Study Human Rotavirus Infection, Host Restriction, and Pathophysiology. *J Virol* **90**, 43-56, doi:JVI.01930-15 [pii];10.1128/JVI.01930-15 [doi] (2015).
27 Kanai, Y. *et al.* Entirely plasmid-based reverse genetics system for rotaviruses. *Proc Natl Acad Sci U S A* **114**, 2349-2354, doi:10.1073/pnas.1618424114 (2017).
28 Philip, A. A. H., B. E.; Garcia, M. L.; Abad, A. T.; Katen, S. P.; Patton, J. T. Collection of recombinant rotaviruses expressing fluorescent reporter proteins. *Microbiol Resour Announc* (2019).
29 Crawford, S. E., Hyser, J. M., Utama, B. & Estes, M. K. Autophagy hijacked through viroporin-activated calcium/calmodulin-dependent kinase kinase-beta signaling is required for rotavirus replication. *Proc Natl Acad Sci U. S. A* **109**, E3405-E3413 (2012).
30 Criglar, J. M. *et al.* A novel form of rotavirus NSP2 and phosphorylation-dependent NSP2-NSP5 interactions are associated with viroplasm assembly. *J Virol* **88**, 786-798, doi:10.1128/JVI.03022-13 (2014).
31 Hyser, J. M., Zeng, C. Q., Beharry, Z., Palzkill, T. & Estes, M. K. Epitope mapping and use of epitope-specific antisera to characterize the VP5* binding site in rotavirus SA11 NSP4. *Virology* **373**, 211-228 (2008).
32 Chang-Graham, A. L. *et al.* Human intestinal enteroids with inducible neurogenin-3 expression as a novel model of gut hormone secretion. *bioRxiv*, 579698, doi:10.1101/579698 (2019).
33 Sato, T. *et al.* Long-term expansion of epithelial organoids from human colon, adenoma, adenocarcinoma, and Barrett's epithelium. *Gastroenterology* **141**, 1762-1772 (2011).
34 Chang-Graham, A. L. *et al.* Human intestinal enteroids with inducible neurogenin-3 expression as a novel model of gut hormone secretion. *Cell Mol Gastroenterol Hepatol*, doi:10.1016/j.jcmgh.2019.04.010 (2019).
35 Ettayebi, K. *et al.* Replication of human noroviruses in stem cell-derived human enteroids. *Science* **353**, 1387-1393, doi:science.aaf5211 [pii];10.1126/science.aaf5211 [doi] (2016).
36 VanDussen, K. L. *et al.* Development of an enhanced human gastrointestinal epithelial culture system to facilitate patient-based assays. *Gut* **64**, 911-920, doi:10.1136/gutjnl-2013-306651 (2015).
37 Estes, M. K., Graham, D. Y., Gerba, C. P. & Smith, E. M. Simian rotavirus SA11 replication in cell cultures. *J Virol* **31**, 810-815 (1979).

38 Matrosovich, M., Matrosovich, T., Garten, W. & Klenk, H. D. New low-viscosity overlay medium for viral plaque assays. *Virol J* **3**, 63, doi:10.1186/1743-422X-3-63 (2006).
39 del Castillo, J. R. *et al.* Rotavirus infection alters Na+ and K+ homeostasis in MA-104 cells. *J Gen. Virol* **72 (Pt 3)**, 541-547 (1991).
40 Zhang, M. *et al.* Mutations in rotavirus nonstructural glycoprotein NSP4 are associated with altered virus virulence. *J Virol* **72**, 3666-3672 (1998).
41 Zhao, Y. *et al.* An expanded palette of genetically encoded Ca(2)(+) indicators. *Science* **333**, 1888-1891, doi:science.1208592 [pii];10.1126/science.1208592 [doi] (2011).
42 Shahrabadi, M. S., Babiuk, L. A. & Lee, P. W. Further analysis of the role of calcium in rotavirus morphogenesis. *Virology* **158**, 103-111 (1987).
43 Motiani, R. K., Stolwijk, J. A., Newton, R. L., Zhang, X. & Trebak, M. Emerging roles of Orai3 in pathophysiology. *Channels. (Austin.)* **7**, 392-401, doi:24960 [pii];10.4161/chan.24960 [doi] (2013).
44 Foulke-Abel, J. *et al.* Human enteroids as an ex-vivo model of host-pathogen interactions in the gastrointestinal tract. *Exp. Biol Med (Maywood.)* **239**, 1124-1134, doi:1535370214529398 [pii];10.1177/1535370214529398 [doi] (2014).
45 Zachos, N. C. *et al.* Human Enteroids/Colonoids and Intestinal Organoids Functionally Recapitulate Normal Intestinal Physiology and Pathophysiology. *J Biol Chem* **291**, 3759-3766, doi:R114.635995 [pii];10.1074/jbc.R114.635995 [doi] (2016).
46 Zhou, Y., Frey, T. K. & Yang, J. J. Viral calciomics: interplays between Ca2+ and virus. *Cell Calcium* **46**, 1-17 (2009).
47 Bhowmick, R. *et al.* Rotaviral enterotoxin nonstructural protein 4 targets mitochondria for activation of apoptosis during infection. *J Biol Chem* **287**, 35004-35020 (2012).
48 Dickman, K. G. *et al.* Rotavirus alters paracellular permeability and energy metabolism in Caco-2 cells. *Am J Physiol Gastrointest Liver Physiol* **279**, G757-766, doi:10.1152/ajpgi.2000.279.4.G757 (2000).
49 Zhu, S. *et al.* Nlrp9b inflammasome restricts rotavirus infection in intestinal epithelial cells. *Nature* **546**, 667-670, doi:10.1038/nature22967 (2017).
50 Zambrano, J. L. *et al.* Rotavirus infection of cells in culture induces activation of RhoA and changes in the actin and tubulin cytoskeleton. *PLoS One* **7**, e47612, doi:10.1371/journal.pone.0047612 [doi];PONE-D-12-19556 [pii] (2012).
51 Hagbom, M. *et al.* Rotavirus stimulates release of serotonin (5-HT) from human enterochromaffin cells and activates brain structures involved in nausea and vomiting. *PLoS Pathog* **7**, e1002115 (2011).
52 Ruiz, M. C. *et al.* Ca2+ permeability of the plasma membrane induced by rotavirus infection in cultured cells is inhibited by tunicamycin and brefeldin A. *Virology* **333**, 54-65 (2005).
53 Crawford, S. E. & Desselberger, U. Lipid droplets form complexes with viroplasms and are crucial for rotavirus replication. *Curr. Opin Virol* **19**, 11-15, doi:S1879-6257(16)30059-1 [pii];10.1016/j.coviro.2016.05.008 [doi] (2016).